ALMA MATER STUDIORUM - UNIVERSITÁ DI BOLOGNA

DEPARTMENT OF PHYSICS AND ASTRONOMY - DIFA

Second cycle degree/two year master in Astrophysics and Cosmology

Exploring the relation between turbulence, gas fluctuations and gravity in the simulated intracluster medium

Master's degree thesis

Candidate:
Marco Simonte

Supervisor:
Prof. Franco Vazza
Prof. Fabrizio Brighenti

Academic year 2019-2020

Abstract

Astrophysical fluids show signs of turbulence across many scales, and turbulent features are also likely to be present in galaxy clusters. The sources of turbulence in galaxy clusters can be several, e.g. following the energetic output from Active Galactic Nuclei or merger events.
In this thesis, we studied the turbulence driven by hierarchical accretion processes, by analysing a sample of galaxy clusters simulated with the cosmological code ENZO. Since one method to study turbulence in galaxy clusters is the observation of surface brightness fluctuations, we investigated the relation between turbulent density and velocity fluctuations. This method is most readily applicable to X-ray data, but is also relevant to Sunyaev-Zeldovich observations. In order to disentagle laminar from turbulent flows, we implemented a fixed scale filtering approach with a 300 kpc filtering scale. We found a statistical relation between the root mean square of density and velocity flucutations, albeit with a different slope than what previously reported in the literature (e.g. Zhuravleva et al., 2014b). In particular, we found a slope smaller than 1, and depending on the dynamical state of the galaxy clusters. Moreover, we investigated the radial trend of turbulent diagnostics, obtaining the density and velocity power spectra at various radii, for the first time in the literature. The slope of the velocity spectra shows a constant trend with radius, and consistent with the Kolmogorov model at all radii. On the othar hand, the slope of the density spectra evolves with radius.
Another process which might affect the density fluctuations is the buoyancy. The Richardson number is a parameter which measures the balance between turbulence and buoyancy, and we found that this variable has a strong dependence on the filtering scale. Moreover, we investigated the relation, recently presented in Mohapatra et al. (2020), between the Richardson number and the logarithmic density fluctuations. In this case, we could not detect any strong relation between the Richardson number and the logarithmic fluctuations, owing to the different distribution of density fluctuations (compared to more simplistic expectations from the literature) in the complex environment of simulated galaxy clusters.

Sommario

La turbolenza è presente in molti ambienti astrofisici e a diverse scale, dalle atmosfere stellari, agli ammassi di galassie. In questi ultimi, le sorgenti di turbolenza possono essere diverse, tra cui turbolenza iniettata da outflow, provenieti da AGN, o merger.
In questa tesi, abbiamo studiato la turbolenza prodotta durante il processo di accrescimento che le strutture cosmiche sperimentano durante la loro evoluzione, analizzando un campione di ammassi di galassie simulati con il codice ENZO. Poichè un possibile approccio allo studio della turbolenza in ammassi di galassie è dato dall'osservazione delle fluttuazioni di brillanza superficiale, abbiamo deciso di approfondire la relazione tra fluttuazioni di velocità e densità generate dalla turbolenza. I risultati sono, perlopiù, applicabili a dati in banda X, ma sono comunque rilevanti per eventuali confronti con osservazioni che utilizzano l'effetto Sunyaev-Zeldovich. Per studiare la turbolenza è necessario separare i moti laminari da quelli turbolenti. Per fare ciò, abbiamo utilizzato un metodo di filtraggio con scala di filtraggio fissa pari a 300 kpc.
Abbiamo osservato una relazione, statisticamente significativa, tra le fluttuazioni di densità e velocità, nonostante il coefficiente angolare sia diverso rispetto ad altri precedenti lavori presenti in letteratura (Zhuravleva et al. 2014b). In particolare, abbiamo ottenuto un coefficiente angolare minore di 1 e il quale mostra una dipendenza in funzione dello stato dinamico dell'ammasso. Inoltre, abbiamo analizzato il profilo radiale delle proprietà della turbolenza, ottenendo lo spettro di potenza sia della velocità, sia della densità a diversi raggi, per la prima volta in letteratura. La pendenza degli spettri della velocità mostra un andamento costante con il raggio ed è in accordo con la teoria di Kolmogorov ad ogni raggio.
Un ulteriore fenomeno che può modificare le fluttuazioni di densità è il buoyancy. Il numero di Richardson è un parametro che tiene in considerazione il rapporto tra turbolenza e buoyancy, e abbiamo osservato che esso dipende dalla scala di filtraggio ipotizzata. Considerando ciò, abbiamo studiato la relazione tra numero di Richardson e fluttuazioni di densità logaritmiche, recentemente presentata da Mohapatra et al. (2020). Nella nostra analisi, non abbiamo ottenuto alcuna relazione significativa tra le due variabili, probabilmente a causa di una differente distribuzione delle fluttuazioni di densità (rispetto a quelle presenti in letteratura) in un plasma complesso come quello presente negli ammassi di galassie.

Contents

1 Introduction

In this chapter we will present a brief overview of the large scale structure formation mechanism in a ΛCDM model, following a recent review by Planelles et al. (2016), and then we will discuss some key properties of the dynamics of galaxy clusters.

1.1 Large scale structure formation

The current hierarchical paradigm of structure formation is the Lambda Cold Dark Matter Model (ΛCDM) with cosmological constant. Different observational probes (Planck Collaboration et al., 2014) have allowed to put constrains on the cosmological parameters and consolidated a picture in which the universe is 13.8 Gyr old with a dark energy component ($\Omega_\Lambda \approx 0.7$), dark matter ($\Omega_{DM} \approx 0.25$) , baryonic matter ($\Omega_b \approx 0.05$) and an Hubble constant $H_0 = 67$ km s^{-1} Mpc^{-1}. The cosmological parameter Ω is defined as the ratio between the (baryon, dark matter, dark energy) density and the critical density of the universe, $\Omega = \frac{\rho}{\rho_{cr}} = \frac{8\pi G\rho}{3H^2}$.
The formation of first structures is driven by the gravitational collapse of small density perturbations of the matter density field. First objects, probably, appeared at z $\sim$ 10-30 and were massive isolated stars (100-300 $M_\odot$) formed in dark matter halos of 10^5 - 10^8 $M_\odot$. In the hierarchical model, the first objects are the building blocks of structure formation, leading to larger galaxies and galaxy clusters trough accretion and merger. A galaxy is an object in approximately dynamical equilibrium, in which there are component (gas, stars, dark matter) interacting with each other. In order to create stars, the gas which falls in the halo must cool, so the first conditions for the birth of a galaxy are the cooling time must be smaller than the free fall time and the density of the gas must be smaller then the critical density, so that the cooling, through line emission, is efficient. Besides, since there are stars, the supernova feedback can play a major role in the evolution of a galaxy ejecting gas out of the system. For this reason, the dark matter halo which hosts the galaxy must be massive enough to keep the gas inside the gravitational well. Galaxy clusters are the largest non linear objects of the universe and, given their deep gravitational potential well, they are extremely important to mark the transition between cosmological and galactic scale. In fact, whereas in the larger structures the evolution is mainly driven by gravity, on galactic scales hydrodynamics is significant as well. The presence of a hot plasma in the galaxy clusters gives us the chance to study a wide range of dynamical processes related to both gravity and baryonic physics. As a consequence, they represent a unique opportunity to answer to a lot of open questions of cosmology and astrophysics. Actually, their number and distribution can be used to place constraints on the current model of cosmic structure formation.
In the following chapters we will briefly summarize the theory of density fluctuations and how their collapse affects the mass function.

1.1.1 Linear theory of density perturbations

The theory of gravitational evolution of small density perturbations, described by Jeans, in an expanding universe, provides a quite exhaustive scenario of cosmic structure formation.
Let us consider an initial density perturbations field, defined by its density contrast

$$\delta(\mathbf{x}) = \frac{\rho(\mathbf{x}) - \bar{\rho}}{\bar{\rho}} \tag{1.1}$$

where $\rho(\mathbf{x})$ is the matter density field and $\bar{\rho}$ the mean mass density. The initial conditions of this field are determined by the inflationary epoch, whose model predicts homogeneous and isotropic gaussian distributed fluctuations.
The evolution of the perturbations is driven by the Friedmann's equation, but, since the dark matter is the dominant component, we can consider a self gravitating, pressureless, non relativistic fluid. With this hypothesis, Newtonian treatment can be applied and the evolution of density fluctuations is described by the continuity, Euler and Poisson equations. If $\delta \ll 1$ these equations result in

$$\frac{\partial^2\delta}{\partial t^2} + 2H(t)\frac{\partial\delta}{\partial t} = 4\pi G\bar{\rho}\delta \tag{1.2}$$

whose solution is

$$\delta(\mathbf{x}) = \delta_+(\mathbf{x},t)D_+(t) + \delta_-(\mathbf{x},t)D_-(t) \tag{1.3}$$

with $D_+(t), D_-(t)$, respectively, the growing and decaying modes of $\delta(\mathbf{x})$ and $\delta_+(\mathbf{x},t), \delta_-(\mathbf{x},t)$ the spatial distributions of fluctuations. These modes depend on the cosmology, so different cosmological parameters means different structure formation history. For example, a universe with $\Omega_m \approx 1$ promotes the collapse and formation of structures, while, on the other hand, with a smaller value (as in the ΛCDM model) there is an epoch when the cosmological constant becomes dominant, providing a cosmic expansion faster than collapse, resulting in a minor number of collapsed structures.
This theory can be applied for the first perturbations with $\delta \ll 1$, and thus cannot be used to study the evolution of structures in non-linear regime, in which case numerical simulations are required.

1.1.2 Non-linear evolution

A model which can explain the non-linear evolution of perturbations is the spherical collapse model. It considers an isolated perturbation which evolves in a background universe, described by an Einstein-de Sitter (EdS) model, which corresponds to a flat universe with $\Omega_{tot} = \Omega_{DM} + \Omega_b = 1$, cosmological constant equal to zero and a cosmological expansion parameter evolving as $a \propto t^{2/3}$. The perturbation grows (with the same law of the background) until it reaches its maximum expansion. At this point the overdensity is $\delta_+ = 4.6$ and if $\Omega_p > 1$ (p means it is related to the perturbation) the condition for the collapse is satisfied. After that, it starts its own different evolution reaching the virial equilibrium when $\rho_p/\rho \simeq 178$. On the contrary, the linear theory would predict a smaller value for the overdensity at the virial time ($\delta_+ \simeq 1.69$).
The spherical collapse is a simple model which can not perfectly describe the total structure formation process. Indeed, during the cosmic evolution, there are a lot of phenomena as the filamentary matter accretion or merger and interactions between density perturbations of different scale which lead to a redistribution of matter. In particular, Genel et al. (2010) have found that the contribution of mergers to the total growth of dark matter halos does not exceed 60 %. This suggests that a significant mass fraction of halos may be accreted in a smoothly way.

1.1.3 Mass function

The mass function is the number density of collapsed objects, at a redshift z, with a mass between M and M+dM in a given volume. Observationally, the mass function is difficult to obtain and numerical simulations are often used to calibrate models and compare with available observational data. Nevertheless, there is an analytical way (Press & Schechter 1974) to determine it. The hypothesis is that any collapsed object with mass ≥ M derives from a density contrast $\delta_M \geq \delta_c$ (critical overdensity for collapse), extrapolated from the linear theory. Considering a spherical collapse, $\delta_c \simeq 1.69$. The initial density fluctuations are gaussian distributed with zero mean and variance σ_M^2. The mass function derived in this way is the Press-Schechter function, and it is in the form

$$\frac{dn(M,z)}{dM} = \sqrt{\frac{2}{\pi}}\frac{\bar{\rho}}{M^2}\frac{\delta_c}{\sigma_M(z)}\left|\frac{dlog\sigma_M(z)}{dlogM}\right| exp\left(-\frac{\delta_c^2}{2\sigma_M(z)^2}\right). \tag{1.4}$$

This mass function is not perfectly in agreement with the one found from cosmological simulations. For this reason, the model has been improved considering the ellipsoidal collapse or non-gaussian fluctuations. Anyway, given the simple assumptions the theory is built on, the accuracy to describe the mass function is limited. Since σ_M depends on cosmological parameters, the mass function and, in particular, its evolution with redshift help to constrain the cosmic evolution model.

1.2 Galaxy clusters properties

Galaxy clusters are the largest virialized systems in the universe and the mass range of these objects is 10^{13} - 10^{15} $M_\odot$. They contain 10^2-10^3 galaxies, in a volume of few Mpc, which have a velocity dispersion $\sigma \approx 10^3$ km/s. Even though the baryon fraction in these systems is about 17 %, the plasma holds the majority of the baryonic mass. The gas temperature is $\sim 10^7$-10^8 K and it emits in the X-Ray band, making clusters one the brightest class of objects at these frequencies with $L_X \approx 10^{43}$-10^{45} erg/s. The intra-cluster medium (ICM) is mostly composed of hydrogen and helium, with an electron density $n_e \approx 10^{-2}$-10^{-4} cm^{-3} and a metallicity that is 1/3 of the solar one.

1.3 Observational features

We summarize some observational features of galaxy clusters, providing a little explanation of the emission mechanism.

- **X-Ray**: since the gas temperature is about $10^7 - 10^8$ K, the main cooling mechanism is the bremsstrahlung in the X-ray band. Nonetheless, line emission is present, due to the abundance of metals in the ICM, as the Fe K_α at 6.4 Kev. In this band is possible to derive the density and temperature profiles and, from the resolved profile of emission lines, the laminar and turbulent velocity of the gas. This allows us to investigate non-thermal processes e.g. turbulence in the ICM medium, but high spectral resolution is required, which has not been achieved so far.
- **Optical band**: the emission at these frequencies is dominated by the black-body emission of stars in the galaxies. In this band it is possible to study random motion of galaxies and their interactions (e.g. ram pressure stripping, high speed encounters). Moreover, it is possible to investigate the galaxy morphological distribution and the evolution of the morphology in clusters and groups.
- **Radio band**: the emission in this band is mostly due to synchrotron process and we can define three different kind of sources: relics, halos and mini halos. First are located in the periphery of the clusters and elongated in the direction perpendicular to the radial one. They probably are generated by shocks, due to merger, which compress the magnetic field extending it along the main major axis. They present polarized radiation. Halos are cluster scale object ($\simeq$ 1 Mpc) and present low surface brightness and polarization. They are associated with perturbed clusters. Mini halos have a typical dimension of 100-500 kpc, with low surface brightness and low polarization and are observed in relaxed clusters. They are, probably, the result of the AGN activity, or minor mergers (Feretti et al. 2012, van Weeren et al. 2019).
  Radio-galaxies, which have a compact radio source associated with the active nucleus, are another contribution to the total radio flux; part of the radio emission is observed in the form of radio lobes, extended regions of emission diametrically opposed with respect to the compact radio source. The energy is carried by a mixture of relativistic and thermal gas, which outlines the jets. In clusters, the rapid motion of the galaxies and the interaction of the gas outflow with the ICM are thought to be responsible for the observed departures from alingment of the radio lobes.

1.3.1 Hydrostatic equilibrium

The ICM is nearly in hydrostatic equilibrium. In fact, let us consider the sound speed $c_s = \sqrt{\frac{\gamma k_B T}{\mu m_p}}$, with γ the adiabatic index (=5/3 for a monoatomic gas), k_B the Boltzman's constant, T is the gas temperature, μ is the mean molecular weight and m_p the proton mass. It is possible to define the sound crossing time of the ICM as $t_s = R/c_s$ with R the typical size of a galaxy cluster. Hence, considering classical parameters for the plasma as T $\approx 10^8$ K and R $\approx$ 1 Mpc, this time scale is shorter than the age of this objects ($t_{age} \approx 10^{10}$ yr). For this reason, the gas can be considered in hydrostatic equilibrium.
One of the most important applications of this property is the cluster mass estimate. Hydrostatic equilibrium means that the pressure of gas is balanced by the gravity force generated by the total mass

$$\nabla\Phi = -\frac{\nabla P}{\rho} \tag{1.5}$$

where Φ is gravitational potential and P is the pressure, obtained from the state equation $P = \frac{\rho k_B T}{\mu m_p}$. Let us assume a spherical simmetry, hence Eq. 1.5 becomes

$$\frac{1}{\rho}\frac{dP}{dr} = -\frac{d\Phi}{dr} = -\frac{GM(r)}{r^2} \tag{1.6}$$

where r is the radius and M(r) the mass within r. If the density and temperature profiles can be determined, it is possible to estimate the total mass of the cluster within the raidus r

$$M(r) = -\frac{k_B T r}{G\mu m_p}\left[\frac{dln\rho}{dlnr} + \frac{dlnT}{dlnr}\right]. \tag{1.7}$$

Both density and temperature profiles are typically obtained from X-ray or radio (through Sunyaev-Zeldovich effect) observations. In particular, the density profile is obtained from the surface brightness and the temperature profile from the cut-off of the bremsstrahlung emission, which is the dominant process for the cooling of the plasma. Observations have confirmed that the ICM has not an isothermal profile, but the shape in the inner region partially depends on the dynamical properties of considered galaxy clusters. Systems which show a decreasing temperature profile towards the core are cool-core (CC) cluster, while the one which show an isothermal profile at the center are non-cool-core (NCC). The difference is plotted in figure 1.1.

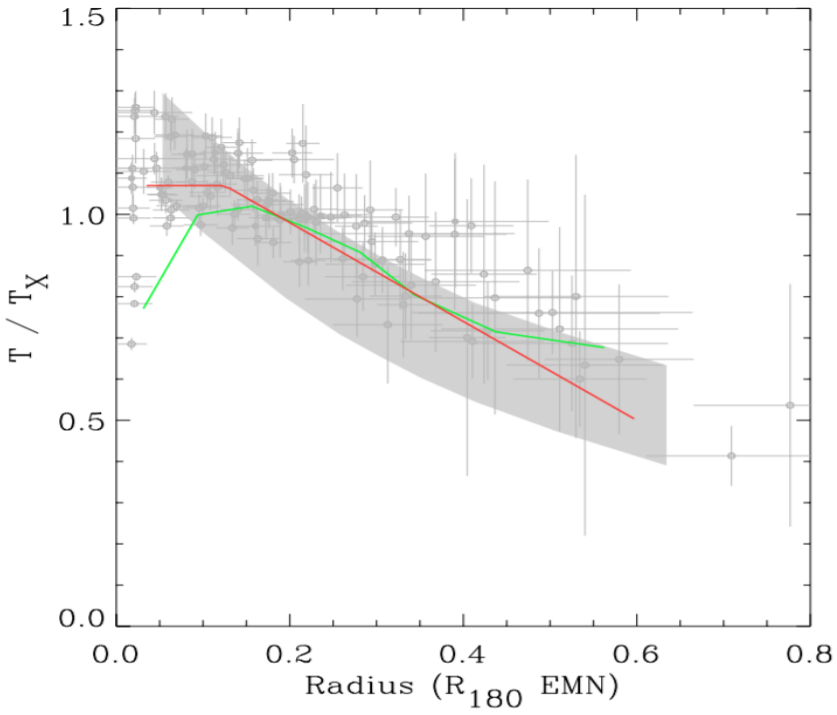

Figure 1.1: *C*omparison of the dimensionless temperature profile from XMM-Newton observations by Pratt et al. 2007 (grey dots with errorbars) with the average profiles from ASCA (grey band, Markevitch et al. 1998), and the observations of cooling core clusters from BeppoSAX (green line, De Grandi & Molendi 2002) and Chandra (red line, Vikhlinin et al. 2005).

A usual density profile is the β model profile (Cavaliere & Fusco-Femiano 1976). The main hypothesis are: spherical symmetry, gas and galaxies subject to the same gravitational potential, isothermal profile (which means constant velocity dispersion profile) and a King's profile for the galaxy distribution. The gas density profile becomes in this case:

$$\rho(r) = \frac{\rho_0}{\left[1 + \left(\frac{r}{r_c}\right)^2\right]^{-3\beta/2}} \tag{1.8}$$

where β is defined as

$$\beta = \frac{\mu m_p \sigma^2}{k_B T} \tag{1.9}$$

and it represents the ratio between kinetic energy of galaxies and thermal energy of the gas. Inserting this profile in the equation 1.7, we obtain

$$M(r) = \frac{k_B r^2}{G\mu m_p}\left[\frac{3\beta T}{r^2 + r_c^2} - \frac{dT}{dr}\right]. \tag{1.10}$$

Both observations (Ettori et al. 2019) and simulations (Angelinelli et al. 2020, Lau et al. 2009) show that hydrostatic mass evaluation underestimates the total mass. Such discrepancy is likely to be explained with the presence of non thermal pressure caused by turbulence and magnetic fields. Due to the importance of the mass measurement of galaxy clusters for cosmology, is fundamental to study the non thermal processes in the ICM and find different methods to evaluate the clusters mass.

1.3.2 Scaling relations

The dominant process in the cosmic structure formation is the accretion driven by gravity. Since the gravity is scale free, all objects of the universe, from galaxy clusters to globular clusters, should have self-similar relations (Kaiser 1986). Nevertheless, the impact of gas physics during the formation and evolution of structures could generate deviations from the theoretical laws. For this reason, observed scaling relations are an important tool to study the thermodynamical history of the ICM and, in general, of the gas in astrophysical objects. In order to present some of the most important relations, we will follow Giodini et al. (2013).
If halos are self-similar in time, two objects which have formed at the same time have the same mean density. Hence

$$\frac{M_{\Delta_z}}{R^3_{\Delta_z}} = constant \tag{1.11}$$

where Δ is the overdensity, defined as the ratio between the density of a system and the critical density of the universe $\rho_{cz} = \frac{3H_z^2}{8\pi G}$, and z is the redshift. Typical values for Δ are 2500, 500, 200 or 100. R_Δ and M_Δ are, respectively, the radius and the mass of the region which has a density contrast equal to Δ

$$M_{\Delta_z} = \frac{4\pi}{3}\Delta_z \rho_{c,0} E_z(z) R^3_{\Delta_z} \tag{1.12}$$

where $E_z(z)=H_z/H_0$ describes the evolution of the Hubble parameter with redshift. As mentioned above, the ICM can be considered in hydrostatic equilibrium, so its temperature provides an estimate of the gravitational potential well

$$T_{gas} \propto \frac{GM}{R} \propto R^2_{vir}. \tag{1.13}$$

Using eq. 1.13 and 1.11 it thus follows that

$$M \propto T_{gas}^{\frac{3}{2}}, \tag{1.14}$$

which is the expected self similar relation between mass and ICM temperature.

A simpler proxy to study the galaxy clusters properties is the X-ray luminosity. In fact, the plasma at a temperature of 10^7-10^8 K mostly emits through bremsstrahlung process, so

$$L_X \propto T^{\frac{1}{2}} \rho_{gas}^2 R_{\Delta_z}^3. \tag{1.15}$$

In this way, it is possible to link the X-ray luminosity and the total mass of clusters.

Another very useful quantity is the gas entropy, defined as $S = \frac{k_B T_{gas}}{n_e^{3/2}}$, so using eq. 1.14 we have the relation between the entropy and the mass.

$$S \propto T_{gas} \propto M^{2/3}. \tag{1.16}$$

As shown in figure 1.2, data do not always follow the theoretical relation scale. A reason might be the variation of gas content in galaxy clusters: in fact there are evidence that the gas fraction decreases with the cluster mass (Vikhlinin et al. 2009). In this way, the L_X-T relation could vary with mass. Another explanation for the deviation from the self-similar prediction is suggested by the complementary analysis of the S-T relation. The theoretical relation (dotted line) does not fit well the data. This suggests a mechanism which can increase entropy or remove gas with low entropy from the center. This can be achieved by non-gravitational processes such as AGN feedback, radiative cooling, star formation or galactic winds. Therefore, all this kind of feedback might heat the gas, resulting in a higher entropy, as Fig. 1.2 shows. This mostly affects galaxy groups due to their smaller gravitational potential well.

The presence of plasma in the galaxy clusters and its interaction with the CMB photons allow us to investigate the properties of these objects in the radio band. The Sunyaev-Zeldovich effect (Sunyaev & Zeldovich 1970) is a process caused by the inverse-Compton scattering of the electrons in the ICM with the CMB photons. The gain of energy of photons is given by

$$\frac{\Delta\nu}{\nu} \simeq \left(\frac{k_B T}{m_e c^2}\right) \tag{1.17}$$

where m_e is electron mass and T the gas temperature. The frequency shift causes an increase in the CMB intensity at high frequencies, and a decrease in the Rayleigh-Jeans tail (as shown in figure 1.3).

The magnitude of decrement in the CMB is a function of the frequency and of the thermodynamical properties of the gas along the line of sight, and it is described by the dimension-less Compton parameter

$$y = \frac{\sigma_T k_B}{m_e c^2} \int n_e T_e \, dl \tag{1.18}$$

where σ_T is the Thompson cross section and the equation gives the total thermal pressure along the line of sight. Observationally, it is useful to define the integrated y-parameter, which is the integral of the Compton parameter over the solid angle under which the cluster is seen, i.e., Ω:

$$Y = \int_\Omega y \, d\Omega = \frac{1}{D_A^2} \frac{\sigma_T k_B}{m_e c^2} \int_V n_e T_e \, dV \tag{1.19}$$

D_A is the angular distance and V the volume of the cluster. In an isothermal scenario this means that

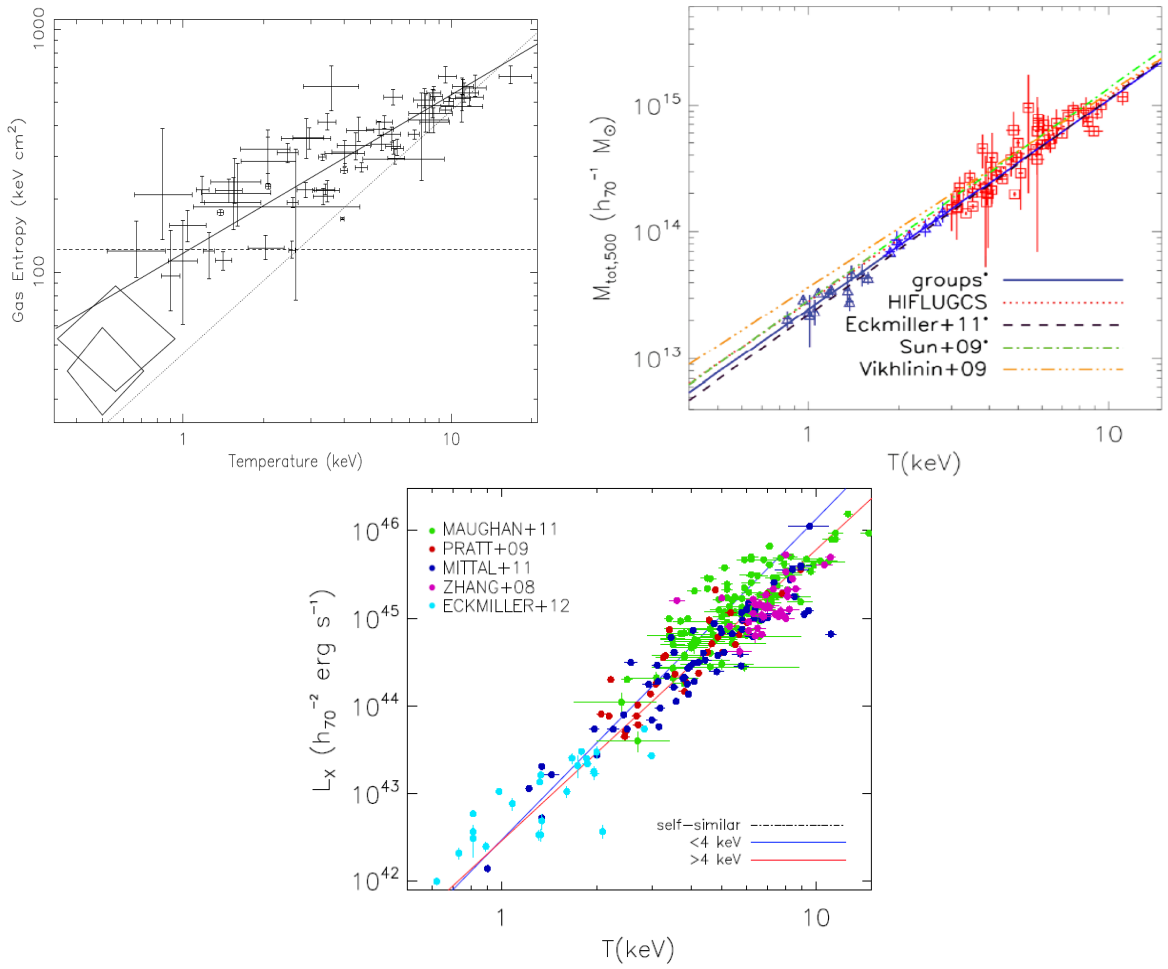

Figure 1.2: Upper-left panel: S-T relation for a sample of clusters. At low temperature the observed clusters does not follow the self-similarity relation. Upper-right panel: M-T relation for groups (blue) and clusters (red). Lower panel: Lx-T relation for different samples of gropus and clusters. All the parameters are evaluated at R_{500}.

$$D_A^2 Y \propto T_e \int_V n_e \, dV \propto f_{gas} M_{tot} T_e \tag{1.20}$$

and using the equation 1.16 we find the relation between Y and M_{tot}

$$D_A^2 Y \propto f_{gas} M_{tot}^{5/3}. \tag{1.21}$$

Kravtsov et al. (2006) proposed an analogue X-ray parameter less affected by non-gravitational processes, whose relation with total mass is plotted in figure 1.4.

Since the scatter of this relation is very small, it provides an optimal proxy for the mass calibration on galaxy clusters. Furthermore, $D_A^2 Y$ is independent of redshift and for this reason SZ effect is used to study galaxy clusters at high redshift and their outskirts.

Observations indicate, in general, that the real situation is very complicated and that we need the numerical simulations to get further insight. They are a good test for the self-similarity theory, since cosmological simulations mainly evolve due to gravity. Nevertheless, the observed deviation needs some

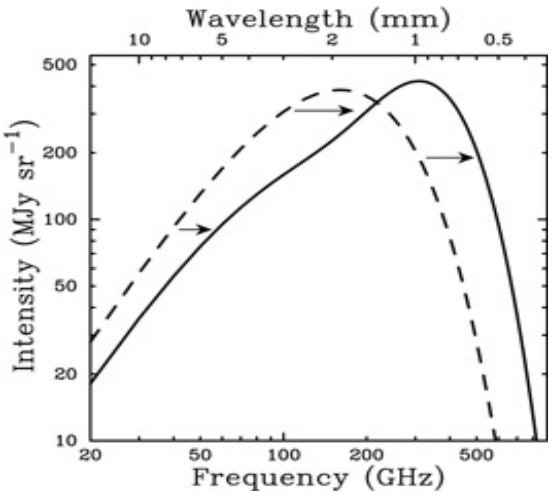

Figure 1.3: The deviation from the CMB black body caused by the S-Z effect. The dashed line represnts the original black body while the solid line traces the spectrum after the interaction.

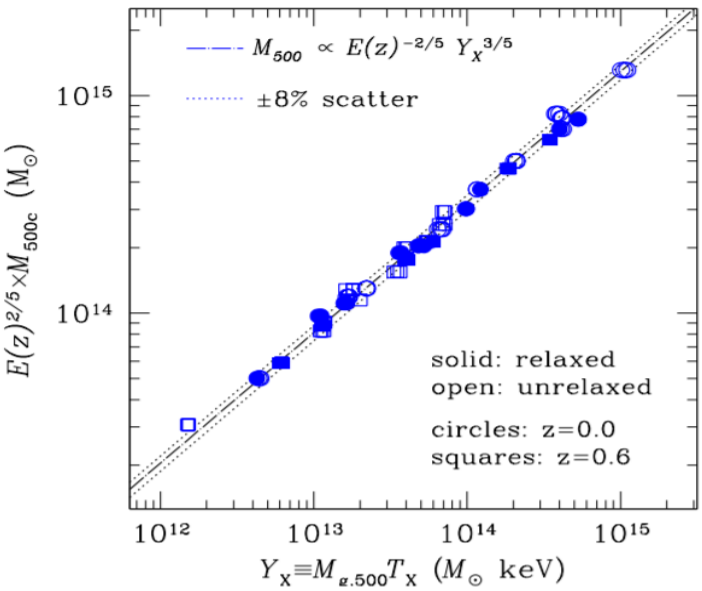

Figure 1.4: M-Y relation from Kravtsov et al. (2006).The dashed line shows the power law relation with the self-similar slope fit to the entire sample. The dotted lines indicate 8% scatter.

other features to include. Radiative cooling is one of the first processes to be taken into account, but it is not sufficient to reproduce the observed relation. Cooling leads to an excessive conversion of gas in stars, promoting a star formation and a significant presence of cold gas which are not observed. A suitable solution is the implementation of a heating mechanism which could come from supernovae or AGN, depending on the host cluster mass. In fact, there are evidence of its impact on the surrounding gas, but some issues (as the coupling between gas and energy emitted by the black hole) are still poorly understood. Another process that could explain the deviation from self-similarity is the pre-heating. In this scenario, the energy injection into the ICM by non-gravitational processes (such as supernovae, star formation, and galactic winds) heats the gas at high redshift, before the gas collapses in the deep cluster/group potential well.

2 Turbulence

In the previous chapter, we have shown that fundamental processes in the formation and evolution of cosmic structures are mergers and accretions of gas and dark matter. These are two of the most energetic phenomena in the universe, with objects that can reach velocities of several thousands of kilometers per second during the interaction. As a consequence, the shocks, generated by such events, inject turbulence in the ICM. Furthermore, we have seen that the hydrostatic model should be revisited by including the residual gas motion produced by non-thermal processes. For these reasons, the ICM is likely to be turbulent. This kind of phenomena should be studied because they are related to a lot of open questions and, also, because turbulence is present at every astrophysical scale, from the surface of stars to galaxy clusters.
The most successful model of turbulence is the "Kolmogorov model", which, under some simple assumptions on the behaviour of the gas, can give results comparable with observations. In this chapter, we will describe the Kolmogorov theory and general properties of turbulence, and then we will focus on turbulence in the intracluster medium.

2.1 Kolmogorov theory

A description of the ICM requires a study of turbulence injected by the continuous gravitational interactions during the whole evolution of the cluster. To completely characterize the physics of turbulence we need numerical simulation, but with under some simple hypothesis, the theory by Kolmogorov (1941) well describes the behaviour of turbulent flows e.g. Pope (2000).

2.1.1 Basic theory

The Kolmogorov theory is based on the idea of the energy cascade, proposed by Richardson (1922). The idea is that the kinetic energy enters the turbulence, trough the production mechanism, at the largest scales of motion. The energy is then transferred by inviscid processes to smaller scales until, at the smallest scales, viscosity dissipates the kinetic energy into thermal energy.
Let us consider a turbulent flow with high Reynolds number, defined as $R_e = \frac{vl}{\nu}$, where ν is the viscosity term and v is the velocity on a scale l. This means that the viscosity may be neglected. In Richardson's view, turbulence can be considered to be composed of eddies of different size l. Each eddy is characterized by a velocity $v(l)$, a timescale $\tau(l) = l/v(l)$ and a Reynolds number $R_e\,(l) = v(l)l/\nu$. The energy cascade continues until the Reynolds number is sufficiently small and the viscosity is effective in dissipating kinetic energy. These eddies have energy of order v^2, so the rate of the transfer of energy can be supposed to scale as $v^2/\tau = v^3/l$.
Kolmogorov added to this scenario some hypothesis. Let us consider a steady state incompressible fluid ($\nabla \cdot \mathbf{v} = 0$). The first hypothesis concerns the isotropy of the small-scale motions. In general, largest eddies are anisotropic and affected by the boundary conditions, but Kolmogorov supposed that the directional biases of the largest scales are lost in the chaotic cascade to smaller scales. Hence:

Kolmogorov's hypothesis of local isotropy; At high Reynolds numbers, the turbulent motions at small scales are statistically isotropic.

As the directional information, the geometry of the largest eddies is also lost. As a consequence, the statistics of the small scales is similar in every turbulent fluid with R_e some large. Since in the energy cascade the dominant processes are the transfer of energy and the viscous dissipation, the parameters that govern the statistically universal state are the dissipation rate of energy ϵ and the kinematic viscosity ν. This leads to the second hypothesis:

Kolmogorov's first similarity hypothesis; In every turbulent flow at high Reynolds number, the

statistics of the small scales have a self-similar form that is uniquely determined by ν and ϵ.

Defining l_{EI} as the scale at which the information on the geometry and direction are lost, the size range $l < l_{EI}$ is referred to as the universal equilibrium range.
Given the two parameters ϵ and ν, a unique length, velocity and time scale can be defined. These are called the Kolmogorov scales:

$$\eta \equiv \left(\nu^3/\epsilon\right)^{\frac{1}{4}} \tag{2.1}$$

$$v_\eta \equiv (\nu\epsilon)^{\frac{1}{4}} \tag{2.2}$$

$$\tau_\eta \equiv (\nu/\epsilon)^{\frac{1}{2}} . \tag{2.3}$$

Considering L_0, v_0 and τ_0, respectively, the size, the velocity and the dynamical time of the largest eddies, and the scaling $\epsilon \sim v_0^3/L_0$, we find, from the above equation, the following results

$$\frac{\eta}{L_0} \propto R_e^{-\frac{3}{4}} \tag{2.4}$$

$$\frac{v_\eta}{v_0} \propto R_e^{-\frac{1}{4}} \tag{2.5}$$

$$\frac{\tau_\eta}{\tau_0} \propto R_e^{-\frac{1}{2}}. \tag{2.6}$$

Evidently, at high Reynolds number the smallest scales are small compared with those of the largest eddies. As a consequence, at sufficiently high Reynolds number, there is a range of scales, l, that are small compared to L_0, and bigger than η, i.e. $\eta \ll l \ll L_0$. This range is called "inertial subrange". Since eddies in this range are much bigger than the dissipative eddies, it may be supposed that their Reynolds number is large and consequently that their motion is little affected by viscosity. Hence:

Kolmogorov's second similarity hypothesis. In every turbulent flow at high Reynolds number, the statistics of the motions at scale l in the range $L_0 \gg l \gg \eta$ have a self-similar form that is uniquely determined by ϵ, independent of ν.

In the inertial subrange, given the size l of the eddy, we can define the other scales in this way

$$v(l) = (\epsilon l)^{\frac{1}{3}} \tag{2.7}$$

$$\tau(l) = \left(\frac{l^2}{\epsilon}\right)^{\frac{1}{3}} . \tag{2.8}$$

A consequence of the second similarity hypothesis is that both v and τ decrease as l decreases.

Once the basic processes of the turbulence cascade are known, it remains to determine the kinetic energy distribution among eddies of different sizes. The simplest statistics containing information about the spatial structure of a random field is the two-point correlation function:

$$R_{i,j}(\mathbf{r}, \mathbf{x}) \equiv \left\langle v_i(\mathbf{x}) v_j(\mathbf{x}+\mathbf{r}) \right\rangle, \tag{2.9}$$

where i and j specify the components of the velocity field and $\mathbf{r}$ is the vector which connects the two points. For homogeneous turbulence $R_{i,j}$ is independent of $\mathbf{x}$.
The velocity spectrum is the Fourier transform of the two-point correlation function

$$\mathbf{U}_{i,j}(\mathbf{k}) = \frac{1}{(2\pi)^3} \iiint_{-\infty}^{\infty} e^{-i\mathbf{k}\cdot\mathbf{r}} R_{i,j}(\mathbf{r})\, d\mathbf{r}, \tag{2.10}$$

where $\mathbf{k}$ is the wavenumber defined as $\mathbf{k} = 2\pi/\mathbf{r}$. A more useful quantity in the wavenumber space is the energy spectrum function (or power spectrum)

$$E(k) = \iiint_{-\infty}^{\infty} \frac{1}{2}\mathbf{U}_{ii}(\mathbf{k})\delta(\mathbf{k}-k)\, d\mathbf{k} \tag{2.11}$$

and the integration of this quantity over all scalar wavenumbers k yields

$$E_K = \int_0^{\infty} E(k)\, dk = \frac{1}{2}\langle v_i v_i \rangle. \tag{2.12}$$

Thus, E(k) represents the contribution to the turbulent kinetic energy from all the modes with $|\mathbf{k}|$ in the range k $\leq |\mathbf{k}| \leq k+dk$. In particular, we are interested in power law spectra of the form $E(k) = Ck^{-p}$, where C is a constant. Consequently, following the Kolgomorov's hypotheses, we can obtain a universal form of the power spectrum. According to the first similarity hypothesis, in the universal equilibrium range, E(k) can be considered a universal function of ν and ϵ. A dimensional analysis shows that the universal relation can be written as

$$E(k) = (\epsilon\nu^5)^{1/4}\phi(k\eta), \tag{2.13}$$

where $\phi(k\eta)$ is a universal non-dimensional function - the Kolmogorov spectrum function. Alternatively, if ϵ and k are used to non-dimensionalize E(k), the relation is

$$E(k) = \epsilon^{2/3}k^{-5/3}\Psi(k\eta), \tag{2.14}$$

where $\Psi(k\eta)$ is the compensated Kolmogorov spectrum function.
According to the second similarity hypothesis, in the inertial subrange, E(k) is uniquely determined by ϵ and it is independent of ν. The latter parameter enters in Eq. 2.14 solely trough η. Hence, the hypothesis implies that as the argument $k\eta$ tends to zero, the function Ψ becomes independent of its argument, i.e. it tends to a constant. In this way, the energy spectrum function is

$$E(k) = C\epsilon^{2/3}k^{-5/3}. \tag{2.15}$$

This relation shows that there is a wide range of scales in which the spectrum can be considered universal, and it is independent of the mechanism responsible of converting kinetic energy into heat through dissipation. In Fig. 2.1 is plotted the Kolmogorov power spectrum, which clearly shows the separation between different ranges of the size of the eddies. At the smaller wavenumbers, k, the power spectrum $E(k) \propto k^2$, while, at the biggest k, turbulence is affected by viscosity which dissipates the kinetic energy generating an exponential cut off.

The dissipation rate ϵ can be derived from the energy spectrum function as follows:

$$\epsilon = \int_0^{\infty} 2\nu k^2 E(k)\, dk, \tag{2.16}$$

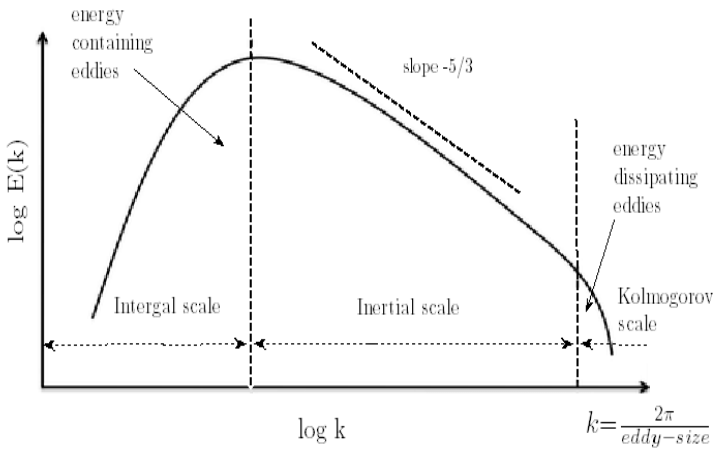

Figure 2.1: Plot of the power spectrum as function of the wavenumber by Sinha (2013). Different ranges are emphasized.

.

thus $2\nu k^2 E(k)$ is the contribution to the disspation rate from the Fourier mode $\mathbf{k}$. In the rest of this thesis, we will look for evidence of a $k^{-5/3}$ power spectrum for the gas velocity field of simulated gas clusters, as a possible signature of turbulence in the ICM.

2.1.2 The evolution of the Fourier modes

Given a function in the real space (e.g. a component of the velocity field) g($\mathbf{x}$), its Fourier series is

$$g(\mathbf{x}) = \sum_k \hat{g}(\mathbf{k}) e^{i\mathbf{k}\cdot\mathbf{x}} \tag{2.17}$$

where $\hat{g}(\mathbf{k})$ is the Fourier coefficient at wavenumber $\mathbf{k}$. These coefficients can be determinded from the orthogonality condition of the Fouries modes $e^{i\mathbf{k}\cdot\mathbf{x}}$. It is convenient to define the operator $\mathcal{F}_k\{\quad\}$ by

$$\mathcal{F}_k\{g(\mathbf{x})\} = \frac{1}{\mathcal{L}^3}\int_0^{\mathcal{L}}\int_0^{\mathcal{L}}\int_0^{\mathcal{L}} g(\mathbf{x}) e^{-i\mathbf{k}\cdot\mathbf{x}}\, d\mathbf{x} = \left\langle g(\mathbf{x}) e^{-i\mathbf{k}\cdot x}\right\rangle_{\mathcal{L}} \tag{2.18}$$

where we denote $\left\langle\quad\right\rangle_{\mathcal{L}}$ the volume average over the cube $0 \le x_i \le \mathcal{L}$.
Applying the operator to the function g($\mathbf{x}$) and exploiting the orthogonality condition of the Fourier modes $e^{i\mathbf{k}\cdot\mathbf{x}}$, we can obtain the Fourier coefficient of the Fourier mode of wavenumber $\mathbf{k}$:

$$\mathcal{F}\{g(\mathbf{x})\} = \left\langle g(\mathbf{x}) e^{-i\mathbf{k}\cdot x}\right\rangle_{\mathcal{L}} = \left\langle \sum_k \hat{g}(\mathbf{k}) e^{i\mathbf{k}\cdot\mathbf{x}} e^{-i\mathbf{k}'\cdot\mathbf{x}})\right\rangle_{\mathcal{L}} = \sum_k \hat{g}(\mathbf{k})\delta_{\mathbf{k},\mathbf{k}'} = \hat{g}(\mathbf{k}'). \tag{2.19}$$

The velocity field $\mathbf{v}$($\mathbf{x}$,t) (and the other quantities related to turbulence) are time dependent. Since the Fourier modes are fixed in time, the Fourier coefficients have a time evolution, which we can study applying the operator $\mathcal{F}_k\{\quad\}$, term by term, to the Navier-Stokes equations:

$$\frac{\partial v_i}{\partial t} + \frac{\partial (v_i v_j)}{\partial x_j} = \nu \frac{\partial^2 v_i}{\partial x_j \partial x_j} - \frac{1}{\rho}\frac{\partial p}{\partial x_j}. \tag{2.20}$$

Considering that $\mathcal{F}_k\{\frac{\partial v_i}{\partial t}\} = \frac{d\hat{v}_i}{dt}$ and $\mathcal{F}_k\{\frac{\partial v_i}{\partial x_i}\} = ik_i\hat{v}_i$, is possible to show that the equation which describes the time evolution of the Fourier coefficients of the velocity field is the following (the dependence on t is implicit)

$$\left(\frac{d}{dt} + \nu k^2\right)\hat{v}_i(\mathbf{k}, t) = -ik_k\left(\delta_{i,j} - \frac{k_i k_j}{k^2}\right)\sum_{k'}\hat{v}_j(\mathbf{k'}, t)\hat{v}_k(\mathbf{k} - \mathbf{k'}, t). \tag{2.21}$$

The viscous term in the left-hand side of the equation has a simple meaning. Let us consider the final period of decay of isotropic turbulence, in which the Reynolds number is so low that the convenction is negligible relative to the effects of viscosity. Then, neglecting the right-hand side of the equation 2.21 and considering an initial condition $\hat{\mathbf{v}}(\mathbf{k}, 0)$ the solution is

$$\hat{\mathbf{v}}(\mathbf{k}, t) = \hat{\mathbf{v}}(\mathbf{k}, 0)e^{-\nu k^2 t}. \tag{2.22}$$

Thus, in the final period of the decay, each Fourier component evolves independently of all other modes, decaying exponentially. In particular, high wavenumber modes decay more rapidly than low wavenumber modes. In contrast, the right-hand side involves **k** and **k'**, which means that in the wavenumber space the convection term is nonlinear and non-local, involving interactions between wavenumbers. As a consequence, in addition to the kinetic energy injected at the biggest scale $l \sim L_0$ (often the size scale of the biggest eddies is equal to the injection scale) and the dissipation term ϵ, there is a term representing the transfer of energy between modes $\hat{T}(\mathbf{k}, t)$. The general equation for the spectral evolution of the turbulence in the Fourier space is

$$\frac{d}{dt}\hat{E}(\mathbf{k}, t) = \hat{T}(\mathbf{k}, t) - 2\nu k^2\hat{E}(\mathbf{k}, t). \tag{2.23}$$

Altough the Kolmogorov theory has a wide range of applications, it has some limits. In particular, most of the astrophysical systems are in the regime of supersonic turbulence. For this reason, more sofisticated analytical and numerical model are required to get a better comprehension of turbulence. Our results (section 4) will indeed highlight the theoretical difficulties in the analysis of the ICM, connected to the presence of supersonic motions.

2.2 Turbulence in the ICM

In the classic picture for the plasma physics, the main mechanism for the energy exchange is the electron-electron (or proton-proton) collision. In this way, considering the Coulomb interactions, Spitzer (1962) found that the electron mean free path is

$$\lambda_e = \frac{3^{\frac{3}{2}}(k_B T)^2}{8\sqrt{\pi}e^4 ln(\Lambda)n_e} \simeq 23\left(\frac{T}{10^8[K]}\right)^2\left(\frac{n_e}{10^{-3}[cm^{-3}]}\right)^{-1}[kpc]. \tag{2.24}$$

Assuming typical values of the temperature and density in the ICM, $\lambda_e \approx 10 - 100$ kpc. Moreover, if the plasma is at the equilibrium, the temperature of the electron is equal to the temperature of the proton, $\lambda_p = \lambda_e$.
The Reynolds number is proportional to the ratio between the inertial and viscous force and can be defined as

$$R_e = \frac{VL}{\nu} = \frac{VL}{\mu/\rho_{gas}} \tag{2.25}$$

where V is the velocity at the scale L and $\mu = \rho_{gas} v_{th}\lambda \approx 6\cdot 10^{-17}\cdot\left(\frac{ln\Lambda}{37}\right)T^{\frac{5}{2}}$ is the viscosity coefficient. Inserting typical galaxy cluster values in the equation 2.25

$$R_e = \frac{VL}{\mu/\rho_{gas}} = \frac{10^8 \cdot 10^6 \cdot 3.08 \cdot 10^{18}}{10^3/10^{-27}} \approx 100. \tag{2.26}$$

A fluid is defined turbulent when $R_e \gg 10$ (say $R_e \approx 10^3$), with lower Reynolds number the instabilities hardly produce turbulence due to the effect of the viscosity.
However, the highly ionized plasma in the galaxy clusters is weakly magnetized (Brunetti & Jones 2014). In this way, the collisionality in the ICM could be mediated by interactions between magnetohydrodynamic waves and the particles, reducing the mean free path from about 10 kpc to fraction of kpc (Beresnyak & Miniati, 2016). The effect is that viscosity (and even the conduction) may be highly suppressed. This hypothesis is supported by some evident features in galaxy clusters as cold front or Kelvin-Helmholtz instabilities. These instabilities would be canceled due to conduction and viscosity in a time scale $\tau \ll \tau_{age}$, where τ_{age} is the age of the galaxy cluster or the time passed from the last merger. The fact they still are present in the ICM is likely to be a sign of the suppression of the mean free path (Roediger et al. 2013, Wang & Markevitch 2018). Considering this new scenario and typical values for clusters we can find that $R_e \gg 10^3$. As a consequence, every little instability can evolve in turbulent motions. This motivates the idea that turbulence can be ubiquitous in galaxy clusters.
Turbulence, thus, could play a fundamental role in lots of unresolved questions about galaxy clusters phenomena. As we have shown turbulence can offer additional non-thermal pressure which can have an impact on the total mass estimation. Furthermore, turbulent diffusion could have an effect on the spread of metals, modifying their radial profiles (Rebusco et al., 2006). Another process in which turbulence could be a key element is the radio emission. In fact, some of the radio structures, are supposed to be powered by turbulent particle acceleration (Brunetti et al. 2008, Cassano 2010) (e.g. "radio halos" in sec. 1.3)

2.2.1 Observational evidence for turbulence in galaxy clusters

In addition to the previous results, there are some observational evidence which support the idea of a turbulent ICM. Schuecker et al. (2004) investigated the merger driven turbulence in the Coma galaxy cluster with the XMM-Newton satellite. They studied the power spectrum of "pseudo"-pressure fluctuations, finding that a power law $P(k) \propto k^{\alpha}$ in the range α = -7/3 to -1/3, is compatible with their measurements. Schuecker et al. (2004) found that the pressure power spectrum between length scale of 40 and 90 kpc is well described by a projected Kolmogorov power spectrum. This suggests that the lower limit for non-thermal pressure support in this scale range is about ~ 10 percent. Using the broadening of the lines in the emitted X-ray spectra of cool-core clusters is possible to put constraints on the fraction of turbulent and thermal energy in the cores of clusters. For the first time in a galaxy cluster, Sanders et al. (2010) place direct limits on the turbulent broadening of the emission lines. They examined the XMM-Newton Reflection Grating Spectrometer (RGS) spectra from the observation of the galaxy cluster Abell 1835. Sanders et al. found from the broadening of the emission line, originating within 30 kpc radius, a velocity of 274 km/s. They also estimated the ratio of turbulent to thermal energy in the core, which is less than 13 %.
Another way to investigate turbulence is by studying the density fluctuations, which result in surface brightness fluctuations in the X-ray band. Sanders & Fabian (2012) studied the surface brightness fluctuations in the cluster AWM 7 in the 0.65 - 5 Kev band. The 3D density power spectrum follows a power law, but with a steeper power index of between -5/3 and -6/3. Besides, Zhuravleva et al. (2014b) argued about the relation between the density and velocity fluctuations in both the buoyancy-dominated regime and turbulent regime. Using high-resolution 3D plasma simulations Gaspari et al. (2014) found a relation between the variance of density perturbations $\delta\rho/\rho$ and the 1D Mach number. Moreover, the authors created X-ray maps to forecast what X-ray telescopes could observe, providing maps of the potential line broadening due to turbulent motions. Finally, Eckert et al. (2017) applied the $\mathcal{M} - \delta\rho$ relation to a sample of 51 galaxy clusters with available radio data to investigate the connection between turbulence and particle acceleration. The authors found a relation linking the radio power at 1.4 GHz and the velocity dispersion, confirming the reliability of the turbulent re-acceleration model.
One of the main results for the internal kinematic of the hot gas was obtained observing the Perseus

cluster with the Hitomi satellite before its sudden failure. In Hitomi Collaboration et al. (2016), studying the iron He-α, He-β and H-like Lyman-α line (fig. 2.2 shows the profiles of these lines), they found that the contribution to the velocity from the turbulent motion is about $\sim$ 160 km/s on scales of $\sim$ 50 kpc. This suggests that the contribution of the turbulent motion to the total pressure in the centre of the cluster is small, with a ratio of turbulent to thermal energy of $\sim$ 4%.
Other observations can also be used to directly infer the amplitude of turbulent motions in the ICM. For example, Rebusco et al. (2006) have examined the metal distribution in galaxy clusters. In particular, the distribution of metals around brightest cluster galaxies is wider than the distribution of the stars which produce them. Assuming that the process responsible for the spread is the turbulent diffusion, they evaluated a diffusion coefficient of the order of 10^{29} cm^2 s^{-1}. From this, one can put constraints on the turbulent velocity, finding a value in the range of $\sim$ 100 km/s on the scale of 10-50 kpc. These observational evidence tell us that the contribution of turbulent motions to the total pressure in the centre of the galaxy clusters is about $\sim$ 10%. Despite this small value, turbulent motions are likely the dominant source of non-thermal energy. The typical value for the turbulent velocity is $\sim$ 100 km/s. As a consequence, the turbulence is subsonic.
However, simulations predict that the turbulent contribution to the total pressure increases at larger radii, but in these regions turbulence is not well constrained observationally as in the centre. Eckert et al. (2019) studied the turbulent properties of the ICM, beyond the virial radius, in order to infer the mass bias. By fixing the baryon fraction within clusters based on numerical simulations, they argued that the required ratio between non-thermal and total pressure is $\sim$ 6% at R_{500} and $\sim$ 10% at R_{200}.

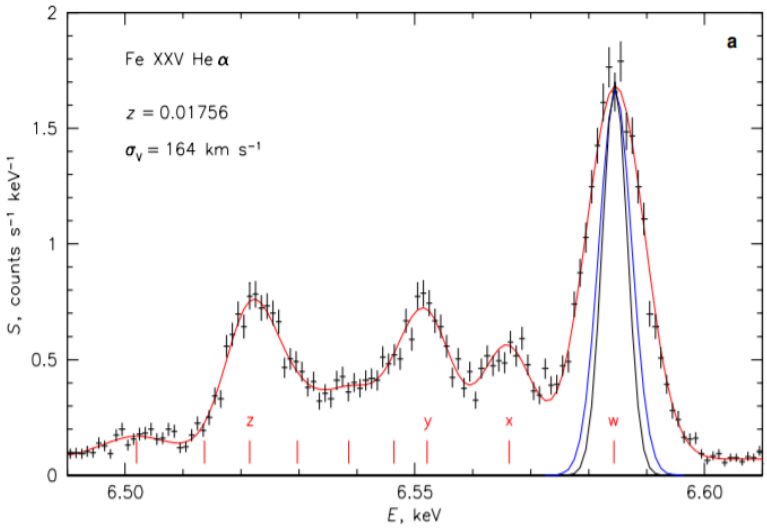

Figure 2.2: Spectra of FeXXV He-α, XXVI Lyman α and XXV He-β from the outer region. Gaussian fits have been made to lines with energies (marked in red) from laboratory measurements in the case of He-like Fe XXV, and theory in the case of Fe XXVI with the same velocity dispersion, except for the He-α resonant line which was allowed to have its own width. Instrumental broadening with (blue line) and without (black line) thermal broadening are indicated. The redshift is the cluster value to which the data were self-calibrated using the He-α lines. Figure from Hitomi Collaboration et al. (2016).

2.2.2 Turbulence driven by cluster merger, Active galactic nuclei and cool-core sloshing

The accretion of gas and dark matter and merger are supposed to be the main mechanism for the evolution of cosmic structure. During these processes, turbulence can be injected in the ICM through shocks and instabilities. For example, figure 2.3 shows two different simulated galaxy clusters in two different dynamical states at z=0.

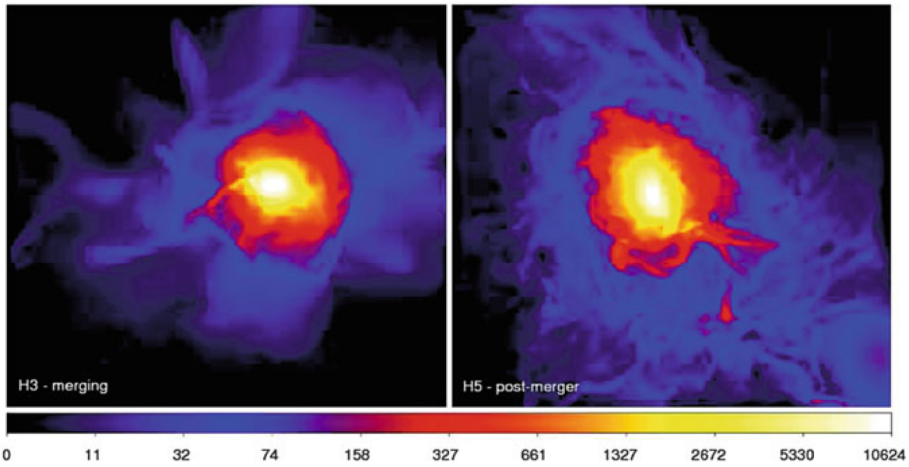

Figure 2.3: map of gas density (in $\rho/\rho_{cr,b}$, where $\rho_{cr,b}$ is the critical baryon density) for a slice of 100 kpc h^{-1} through the centre of the major merger cluster H5 (right column) and of the merging cluster H3 (left column). Maps from Vazza et al. (2012).

Vazza et al. (2011) found that the volume filling factor of the turbulence motions below a scale of $\sim$ 300 kpc is relatively small: it seems to be $\sim 30\%$ for the central part of post-merger clusters and $\sim 5\%$ within the same volume for the relaxed systems. During the accretion some shocks can be generated due to the high velocities of the interacting systems, even if the Mach number is not large (Ryu & Kang, 2003). Vazza et al. (2017) studied turbulence generated by cluster formation. They detected shocks using the algorithm presented in Vazza et al. (2009a) in order to avoid spurious term induced by this event and decomposed the filtered velocity field into solenoidal and compressive motions (see Vazza et al., 2012, for an example of filtering techinque). Vazza et al. found that shocks affect both solenoidal and compressive velocity components, but the dissipation in compressive modes is less important. In particular, they only account a few per cent of the total turbulent dissipation rate in the central $\sim Mpc^3$ volume, while the contribution increases to $\sim 15\%$ within the same volume during the merger events, and to $\sim 30\%$ in the cluster outskirts.

Merger events could, also, trigger the production of cold front, which consists in a discontinuity in X-ray brightness and gas temperature. They are divided into two classes: merger cold fronts, which are the contact discontinuities that are formed between the intra-cluster media of the two merging clusters, and sloshing cold fronts. The latter are the result of the displacement of the cluster core, from the centre of the gravitational potential, due to the interaction with a sub-cluster. As a consequence, the gas falls back and start sloshing inside the gravitational potential well. The superimposition of sloshing and hydrodynamical instabilities (as Kelvin-Helmholtz instability) could inject turbulence in the ICM. It is important to evaluate the amount of small-scale turbulent motions because turbulence present along the cold front has been proposed as a mechanism to accelerate particles and create radio mini-halos (see ZuHone et al., 2011).

Another source of turbulence in the ICM comes from the powerful outflows from active galactic nuclei. It has been shown that the AGN feedback is a key process in the evolution of galaxies and galaxy clusters (Brighenti & Mathews 2002, Gaspari et al. 2011a). Gaspari et al. (2011b) proposed a Chaotic Cold Accretion (CCA) model in which the hot gas is organized in hot gaseous halos, while hot gas and neutral medium are combined to form filaments of warm gas. The authors showed how this scenario has an accretion which is 100 times more efficient than the Bondi's accretion. In particular, AGN feedback can play an important role in mixing metals and removing cold and low-entropy plasma from the center. Li et al. (2020) used high-resolution optical data to study the turbulence injected by AGN feedback, showing that the multi-phase filamentary structures are turbulent. This suggests that turbulence could

be an important channel for the energy exchange between the AGN feedback and the ICM.
While turbulence injected by cluster merger may fill the whole volume of the galaxy clusters, turbulence driven by the AGN feedback mostly affects the innermost region.
It is important to constrain the parameters of the turbulence because the dissipation on the smallest scale has been proposed as a mechanism which can heat the ICM (Zhuravleva et al., 2014a). The turbulence heating rate can be estimated as

$$Q_{turb} = C\rho\frac{v^3}{L} \tag{2.27}$$

where C is a constant, ρ is the gas density and v is the velocity at the scale L. Zhuravleva et al. found that, in the Perseus and Virgo cluster, the local Q_{turb} balances the local cooling rate as shown in figure 2.4.

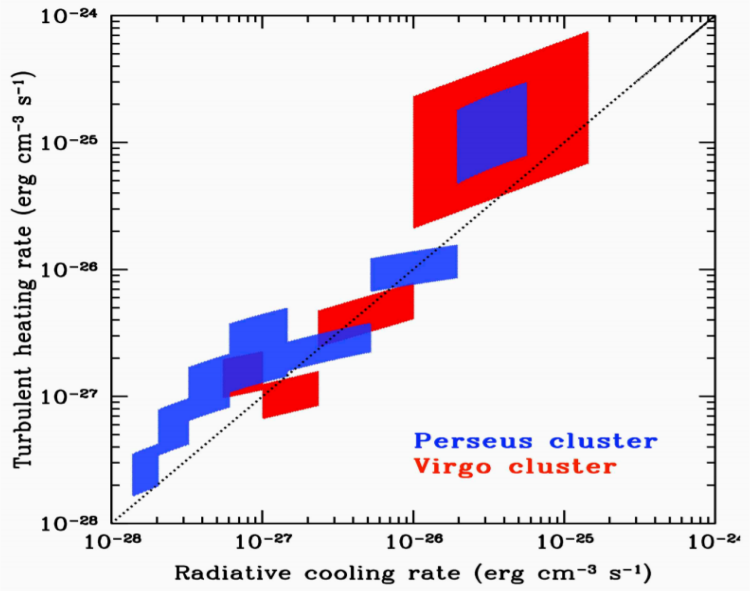

Figure 2.4: Turbulent heating versus gas cooling rates in the Perseus and Virgo cores, taken from Zhuravleva et al. (2014a). Each shaded rectangle shows the heating and cooling rates estimated within a given annulus. The size of each rectangle gives the 1σ uncertainty.

Despite this, Reynolds et al. (2015) found that less than 1% of the total energy ejected by the AGN ends up in turbulence, making this heating mechanism inefficient. The Hitomi Collaboration et al. (2016) estimated a turbulent velocity of about $\sim$ 160 km/s on a scale of 10-50 kpc, resulting in a heating rate that cannot balance the cooling rate in the Perseus cluster. Therefore, the topic still debated.
Another topic of interest is the estimation of turbulence diffusion, which can be evaluated once turbulence velocity and scale are estimated:

$$D \approx \frac{1}{3}\lambda v_{turb} \tag{2.28}$$

where λ is the mean free path in the ICM and v_{turb} the turbulent velocity. Vazza et al. (2012) obtained the distribution of turbulent diffusion from mergers, AGN activity and cool-core sloshing, plotted in fig. 2.5.

The authors found that the most efficient turbulent mechanism to spread metals or particles is that generated by cluster mergers and accretion, which injects turbulence in the whole volume of galaxy clusters. In this case the turbulent diffusion has a distribution with a maximum at D $\sim 10^{29}-10^{30}$ cm^{2}s^{-1}. On the other hand, cool-core sloshing and AGN feedback are less efficient; the distribution of D has

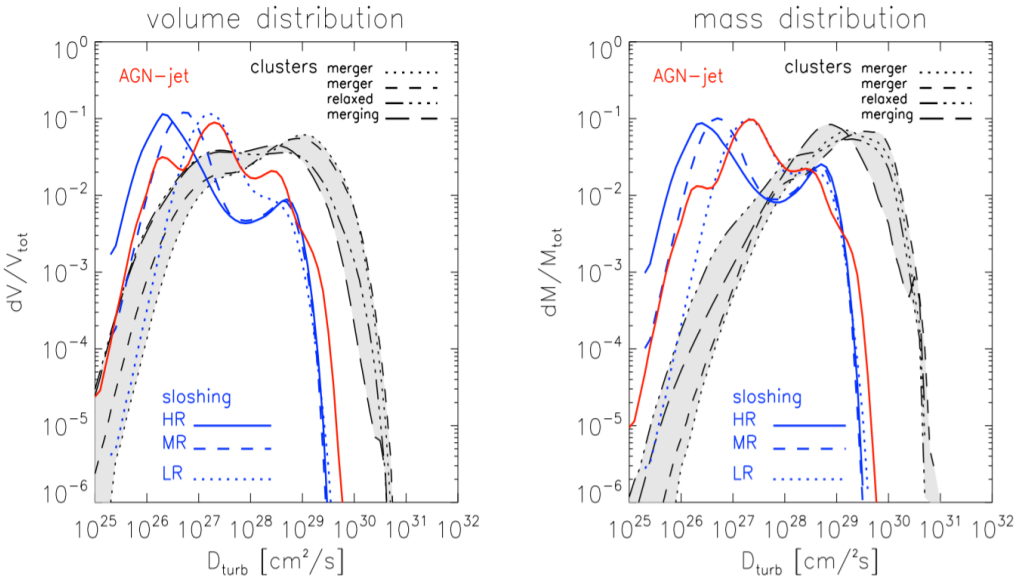

Figure 2.5: Volume (left) and mass (right) distribution of turbulent diffusion in simulated galaxy clusters. In red the turbulent diffusion from the AGN-jet is shown, in blue the distributions of turbulent diffusion from the sloshing and in black the turbulent diffusion from cosmological clusters. The different line-styles are for each different object while the shadowed region shows the uncertainty in the overall cluster sample. Plot from Vazza et al. (2012).

maxima at smaller values $D \sim 10^{26} - 10^{27}$ cm^{2}s^{-1}. There is a second maximum at $D \sim 10^{29}$ cm^{2}s^{-1} but with smaller volume filling factor.

2.2.3 Previous results from simulations

The first simulations of merging clusters have been performed by Evrard (1990) and Thomas & Couchman (1992), who found that shocks play an important role in the evolution of cosmic structures. Schindler & Muller (1993) for the first time developed an eulerian PPM scheme to study the gas dynamics in an idealised merger. In this work, the authors estimated the X-ray emission and presented the X-ray temperature map. Norman & Bryan (1999) studied turbulence in the ICM using the Piecewise Parabolic Method (PPM) on fixed and adaptive meshes which allow them to resolve the flow field in the intracluster gas. They found that turbulence is mildly supersonic with Mach number $\mathcal{M} \sim 1.6$ near the virial radius, while it is subsonic in the innermost region of the galaxy cluster. In this work turbulent velocities are found to vary with radius, being $\sim 25\%$ of σ_{vir} in the core (where σ_{vir} is the value of the velocity dispersion at the virial radius), increasing to $\sim 60\%$ to the virial radius. The authors, also, argued that the mechanism which can sustain the obtained level of turbulence are the frequent minor mergers, rather than major mergers.
Kim & Ryu (2005) studied the density power spectra of transonic and supersonic turbulent flows through one- and three-dimensional simulations. They found Kolmogorov spectra for low Mach number, while the slope flattened increasing the Mach number.
The study of turbulence in cosmological simulations has been pioneered by Dolag et al. (2005) using a smoothed particle hydrodynamics (SPH) code. They introduced a scheme in which viscosity increases near shocks and decaying after passing trough them. The authors found that the kinetic energy associated with turbulent gas motion can be up to 30 per cent of the thermal energy content in galaxy clusters with $\sim 10^{15} M_{\odot}$. This value can increase up to 50 % in the innermost region (even if later studies revised this number). On the other hand, the ratio between thermal and turbulent energy is up to 5 % in clusters with $10^{14} M_{\odot}$. Besides, the amount of turbulent energy released by accretion and mergers is enough to

power the radio emission observed in many galaxy clusters.
In order to shed light on the properties of turbulent motions in more "realistic" galaxy clusters, it is required a decomposition in the bulk and turbulent component of the velocity field. With the aim to achieve this, many methods have been implemented. Lau et al. (2009) estimated the turbulent velocities as the residual respect to the ICM velocity field, averaged over spherical shell. They studied the hydrostatic mass bias in simulated galaxy clusters and found that gas motions contribute up to $\sim$ 5%–15% of the pressure support in relaxed clusters, which leads to the underestimate of the total virial mass accounting only for the thermal pressure. In more detail, the bias is about 6% $\pm$ 2% at R_{2500} and 8% $\pm$ 2% at R_{500} in relaxed system, increasing, in perturbed system, to 9% $\pm$ 3% and 11% $\pm$ 6% at these radii, respectively. Alternatively, one can estimate the turbulent motions interpolating the original 3-D velocity field to map the local mean field and to detect the turbulent fluctuation on scales smaller than the interpolation scale (Vazza et al. 2009b, 2011). Vazza et al. (2012) have proposed a multi-scale iterative filtering of the 3D velocity field, with which the authors studied the turbulence injected by AGN, merger and cold fronts, covering a large range scale (1 kpc to 1 Mpc). An example of this filtering approach is shown in fig. 2.6. In the top left panel is mapped the total velocity field, while in the other panels is plotted the velocity field after applying the multi scale filter and a filter with fixed scale.

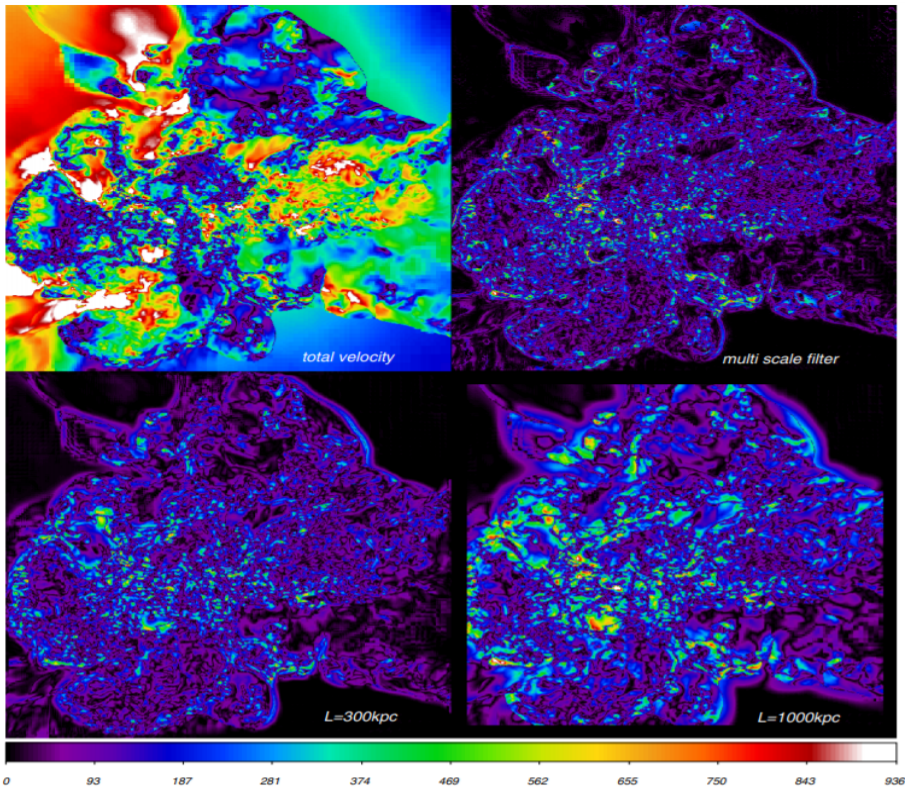

Figure 2.6: Two-dimensional maps of total gas velocity fields (Vazza et al. 2012). Top left total gas velocity (in [km s^{-1}]); top right turbulent velocity field captured by our new multi-scale filter; bottom left turbulent velocity field after the removal of L $\geq$ 300 kpc scale; bottom right turbulent velocity field after the removal of L $\geq$ 1000 kpc scales.

The main results are that the ratio between turbulent and thermal energy $E_{turb}/E_{th} \sim 0.1 - 0.3$ in the innermost region of the clusters. On the other hand, more relaxed systems have much lower values of the turbulent ratio, $E_{turb}/E_{th} < 0.1$. Moreover, the power spectra have a Kolmogorov power index $\alpha \sim 5/3$ or steeper. Miniati (2015) and Vazza et al. (2017) have found that the solenoidal turbulence with a Kolmogorov spectrum dominates the central region of clusters, while the compressible component becomes more important towards the outskirt.
Finally, Angelinelli et al. (2020) studied a sample of galaxy clusters simulated with the ENZO code in

order to test the goodness of the estimate of the total galaxy cluster mass via the hydrostatic equilibrium hypothesis. They estimated the ratio between turbulent and total pressure $\alpha = P_{nt}/P_{tot}$ by comparing the mass estimated from the hydrostatic equilibrium equation with the total mass distribution. The authors found that the median in the sample is $\alpha \sim 10 - 20\%$ at R_{500} and R_{200}.
Despite the high resolutions, the most recent simulations do not resolve the length scale of physical turbulent dissipation. For this reason, subgrid model which incorporate the evolution of turbulence at this scale have been developed.

2.2.4 On the balance between gravity and turbulence

Studies on turbulence in astrophysical systems often consider an idealised Kolmogorov picture in which turbulence is homogeneous and isotropic. However, the stratification present in the ICM makes the analysis more complicated as gravity affects the gas dynamics. Due to the lack of X-ray telescopes with high spectral energy resolutions, many observational studies infer information on the turbulent velocities starting from the density fluctuations. Stratification can, thus, change the interpretation of important statistical tools used to analyse turbulence. In the ICM, energy can be channeled back and forth between kinetic energy and gravitational potential energy, resulting in possible variations on the rate of transfer of kinetic energy at a given scale. Moreover, there are multiple kinds of density fluctuations, due to the action of the buoyancy force. When a parcel of gas moves to higher (lower) radii, it has higher (lower) density compared to the local profile and appears as positive (negative) over-density at the new location of the parcel.
Since the role of buoyancy in the stratified ICM is center to this thesis, we shortly review its formal modelling. Let us consider a parcel of gas with density ρ' and pressure P' at a given radius r. If we adiabatically perturb the parcel, rising it to r+dr, the change in pressure and density are, respectively,

$$\Delta P' = P'(r + dr) - P(r) = \frac{\partial P}{\partial r} dr, \tag{2.29}$$

$$\Delta \rho' = \left(\frac{\partial \rho'}{\partial P'} \right)_S \Delta P'. \tag{2.30}$$

Since the the density of the environment $\rho(r)$ changes as a function of r, the overdensity is

$$\delta \rho = \frac{dP}{dr} \left[\left(\frac{\partial \rho'}{\partial P'} \right)_S - \frac{\partial \rho}{\partial P} \right] \delta r. \tag{2.31}$$

The buoyancy restoring force introduces a new time-scale to the system, which is characterized by the Brunt-Väisälä (BV) frequency, which is defined as

$$N_{BV} = \sqrt{-\frac{g}{\gamma} \frac{dln\left(P/\rho^{\gamma}\right)}{dr}} \tag{2.32}$$

where g is the gravitational acceleration, γ the adiabatic index and P and ρ the gas pressure and density respectively. The BV frequency is a measure of the stability of stratified fluids in which a mass of gas is adiabatically perturbed in the vertical direction; in particular, if $N_{BV}^2 > 0$ the fluid is stable.
An important proxy describing the relative strength of the buoyancy force compared to the inertia of the turbulence is the Richardson number, defined as:

$$R_i = \frac{N_{BV}^2}{\left(v_l/l\right)^2} \tag{2.33}$$

where v_l is the turbulent velocity at the scale l. Therefore, the Richardson number may be seen as the ratio between the BV frequency and the typical turbulence eddy turn-over time scale. Generally

speaking, $R_i > 1$ (buoyancy time < turbulence eddy turn-over time) suggests that the buoyancy force becomes dynamically important, whereas $R_i \ll 1$ (buoyancy time $\gg$ turbulence eddy turn-over time) suggests homogeneous isotropic turbulence unaffected by density stratification.
Recent works investigated the role of the stratification in the ICM. Shi & Zhang (2019) performed an idelised simulation in order to study how the turbulent properties change in a stratified medium. The authors found mildly-stratified plasma with a Froude number $F_r = R_i^{-1/2} \sim 1$, which decreases to $F_r \sim 0.1$ in the central region. Nevertheless, the Froude number is still larger than the condition $F_r < 0.1$ commonly used to identify strongly-stratified turbulence. Besides for $F_r \sim 0.3$, such a stratification influences the morphology of the turbulent eddies, developing vertically thin and horizontally extended pancake-like structures.
Valdarnini (2019) analysed a large set of N-body/SPH hydrodynamical cluster simulations, finding a Froude number $F_r < 0.1$ within $r/r_{vir} < 0.1$. This result suggests that in the cluster core ICM turbulence is strongly modified by the presence of the gravity buoyancy force which suppresses the motions along the radial direction.
Mohapatra et al. (2020) have recently studied the strength of the density fluctuations as function of the Richardson number. They found a relation which involves the Mach number $\mathcal{M}$, the Richardson number R_i and the scale height of the pressure H_p and entropy H_s

$$\sigma_s^2 = ln\left(1 + b^2\mathcal{M}^4 + \zeta^2\mathcal{M}^2 R_i \frac{H_p}{H_s}\right), \tag{2.34}$$

where σ_s^2 is the width of the pdf of the variable $s = ln\,(\rho/\bar{\rho}_z)$. The Richardson number in this work is in the range of $\sim 10^{-4} - 10$ and they found that the amplitude of density fluctuations increases as a function of R_i for $0.01 < Ri < 10$, reaches the peak at $R_i \approx 10$ and starts decreasing at $R_i > 10$ (fig 2.7).

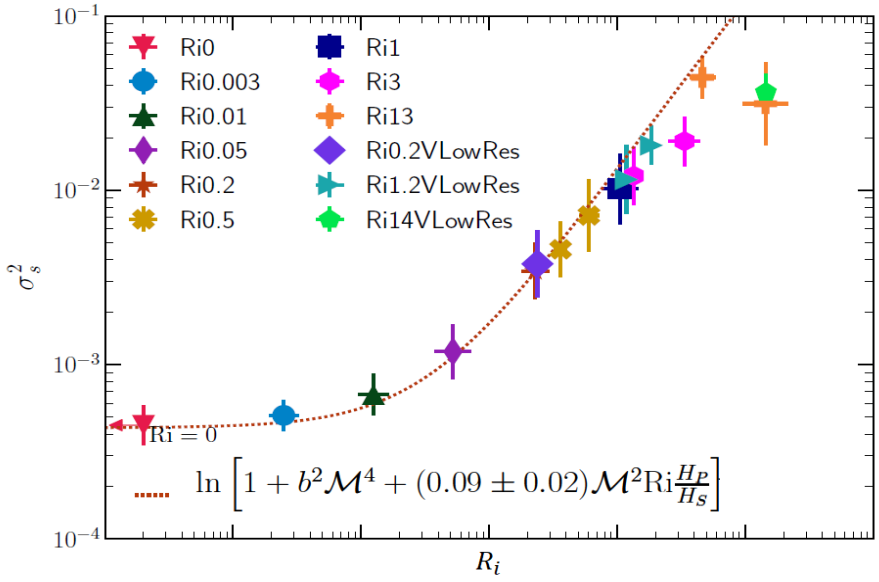

Figure 2.7: Scatter plot of σ_s^2 versus R_i. Plot from the paper Mohapatra et al. (2020).

My thesis aims at testing the validity of the above picture in the more complex and time variable ICM of simulated galaxy clusters obtained from a cosmological simulation (see sec. 4.3).

3 The cluster sample

In this work, we analysed a sample of simulated galaxy clusters from the "Itasca Simulated Clusters" set of simulations. The simulation was carried out at high spatial resolution with Adaptive Mesh Refinement (AMR) and the Piecewise Parabolic Method (PPM) in the ENZO fluid dynamics code (Bryan et al. 2014, see below).

3.1 ENZO code

ENZO is a (parabolic) cosmological numerical code for magneto-hydrodynamics. The main feature of the ENZO code is its Adaptive Mesh Refinement (AMR) capability which allows reaching extremely large spatial and temporal dynamical range. This method utilizes an adaptive hierarchy of grids at different levels of resolution. In this way, starting from the root grid, which covers the entire volume with a coarse uniform grid, one can place finer grids as soon as interesting regions start to evolve. These refined patches may require further refinement, resulting in a hierarchical structure that can continue to any depth. As the evolution continues, it may be necessary to move, resize or even remove the finer mesh. In this way, if the root grid spacing is Δx, then the spacing of a refined patch at level l is $\Delta x/r^l$, where r is the integer refinement factor.
The fluxes across cells in the simulated grid are governed by the following Eulerian equations of the ideal magneto-hydrodynamics, including gravity, in a coordinate systems comoving with the cosmological expansion:

$$\frac{\partial \rho}{\partial t} + \frac{1}{a}\nabla \cdot (\mathbf{v}\rho) = 0, \tag{3.1}$$

$$\frac{\partial \rho \mathbf{v}}{\partial t} + \frac{1}{a}\nabla \cdot \left(\rho \mathbf{v}\mathbf{v} + \mathbf{I}p^* - \frac{\mathbf{B}\mathbf{B}}{a}\right) = -\frac{\dot{a}}{a}\rho\mathbf{v} - \frac{1}{a}\rho\nabla\Phi, \tag{3.2}$$

$$\frac{\partial E}{\partial t} + \frac{1}{a}\nabla \cdot \left[(E + p^*)\,\mathbf{v} - \frac{1}{a}\mathbf{B}\,(\mathbf{B}\cdot\mathbf{v})\right] = -\frac{\dot{a}}{a}\left(2E - \frac{\mathbf{B}^2}{2a}\right) - \frac{\rho}{a}\mathbf{v}\cdot\nabla\Phi - \Lambda + \Gamma + \frac{1}{a^2}\nabla\cdot\mathbf{F}_{cond}, \tag{3.3}$$

$$\frac{\partial \mathbf{B}}{\partial t} - \frac{1}{a}\nabla \times (\mathbf{B}\times\mathbf{v}) = 0. \tag{3.4}$$

In this equations, ρ, $\mathbf{v}$ and a are the comoving gas density, peculiar velocity and the cosmological expansion parameter, respectively. E, $\mathbf{B}$ and p* are the total comoving energy, the comoving magnetic field strength and the total pressure (thermal plus magnetic). The first equation represents the conservation of mass and the second the conservation of the momentum. In the energy conservation equation (third) there are Λ, Γ and $\mathbf{F}_{cond}$ that are radiative cooling, radiative heating and the flux due to thermal heat conduction respectively. The system of equations is closed by the equation of state for an ideal gas with adiabatic index γ and the Poisson's equation for the gravitational potential Φ:

$$e = \frac{p}{\gamma - 1} \tag{3.5}$$

$$\nabla^2\Phi = \frac{4\pi G}{a}\left(\rho_{total} - \rho_0\right). \tag{3.6}$$

Here, e is the comoving thermal energy density and G the gravitational constant. The gravitational potential is created by the total mass denisty contrast, evaluated as the difference between $\rho_{total} = \rho_{DM} + \rho_* + \rho_{gas}$ and the mean density ρ_0.

The evolution of $a(t)$ is governed by the second Friedmann equation for the expansion of a spatially homogeneous and isotropic universe

$$\frac{\ddot{a}}{a} = -\frac{4\pi G}{3a^3}\left(\rho_0 + \frac{3p_0}{c^2}\right) + \frac{\Lambda_c c^2}{3}, \tag{3.7}$$

where ρ_0 is the mean comoving mass density, p_0 is the comoving pressure offered by the background, and Λ_c is the cosmological constant.

To solve the magneto-hydrodynamical equations several solvers are implemented in ENZO. The simulations studied in this thesis are purely hydrodynamical (e.g. without magnetic field) and are based on the Godunov PPM scheme (Colella & Woodward 1984). These are the steps that the scheme follows:

1. Perform a monotonic parabolic interpolation of cell average data, for all the hydrodynamical quantities.
2. Compute the state of each interface averaging the parabola in the domain of the interface.
3. Solving the Riemann problem given interface data.
4. Update the cell average fluid quantities estimating the flux difference at the interface.

The method is second-order accurate both in time and space.
Concerning the gravitational part of the code, the Poisson's equation is solved using fast Fourier technique (Hockney & Eastwood 1988), on the root grid on each time step. In this way, it is implemented a fast and accurate method which allows periodic boundary conditions.
In cosmological simulations there is, also, the collisionless matter (e.g. dark matter, stars) which is modelled with particles which interact only via gravity and whose dynamics is governed by Newton's equation:

$$\frac{d\mathbf{x}}{dt} = \frac{1}{a}\mathbf{v} \tag{3.8}$$

$$\frac{d\mathbf{v}}{dt} = -\frac{\dot{a}}{a}\mathbf{v} - \frac{1}{a}\nabla\Phi. \tag{3.9}$$

In the code, the trajectories of these particles are obtained using a kick-drift-kick algorithm with second-order accuracy even in the presence of varying time steps. Particles are stored in the most highly refined grid patch at the point in space where they exist.

3.2 Our simulations

The cosmological simulations of the Itasca sample assume the WMAP7 ΛCDM cosmology (Komatsu et al. 2011), with $\Omega_B = 0.0445$, $\Omega_{DM} = 0.2265$, $\Omega_\Lambda = 0.728$, Hubble parameter $h = 0.702$, $\sigma_8 = 0.8$ and a primordial index of $n = 0.961$. All runs were non radiative, i.e. they did not consider the gas cooling or the heating from star forming regions or active galactic nuclei. Despite the effects of non-gravitational heating are limited, on the $\gg 100$ kpc scales, compared to the merger or accretion impact in the ICM (Valdarnini 2019), however, the combination of cooling and feedback can increase the number of dense substructures. This implies that the estimation of the gas density and temperature could be locally biased. Besides, an enhanced number of substructures with different temperature and density could produce, with the help of instabilities, small-scale turbulent motions.
The simulations were runned with the following procedure:

ID	$M_{200}\ [10^{14} M_{\odot}]$	$R_{200}[Mpc]$	Dyn. status (w)	Dyn. Status (c)
IT90_0	0.88	0.88	Perturbed	Perturbed
IT90_1	2.45	1.29	Relaxed	Perturbed
IT90_2	1.10	0.99	Relaxed	Perturbed
IT90_3	0.72	0.86	Perturbed	Perturbed
IT90_4	0.54	0.78	Perturbed	Perturbed
IT92_0	3.32	1.42	Relaxed	Perturbed
IT92_1	1.00	0.96	Perturbed	Relaxed
IT92_2	1.17	1.01	Perturbed	Relaxed

Table 1: List of the clusters of our sample with their main properties

- Independent cosmological volumes were simulated in order to select the most massive objects in the volume. Initial conditions were generated, separately for each simulations, at redshift z = 30. The spatial resolution, at this level, is $L_0 = 110$ h kpc$^{-1} \approx 157$ kpc and the DM mass resolution is $m_{DM} = 8.96 \cdot 10^7$ M$_{\odot}$.
- A second more refined grid was created, centered on the cluster formation region, which covered the innermost ≈ 31 Mpc. In this case, the spatial resolution reaches 55 h kpc$^{-1} \approx 78.4$ kpc and the DM mass resolution is $m_{DM} = 1.12 \cdot 10^7$ M$_{\odot}$.
- Inside the central $(L_0/10)^3 \approx 6.3$ Mpc^3 volume of each box a fixed further refinement was enforced. This volume is large enough to include the virial radii of most of the clusters and the spatial resolution increases to 13.8 h kpc$^{-1} \approx 20$ kpc.

The full "Itasca simulated cluster" sample consists of 20 galaxy clusters with the above resolutions and is used to investigate almost every dynamic and thermal properties of the ICM. In this thesis, I used 8 clusters at z = 0, with $0.54 \cdot 10^{14}$ M$_{\odot}$ < M$_{200}$ < $3.32 \cdot 10^{14}$ M$_{\odot}$. In table 1 we report the main properties of the galaxy clusters sample. The analysis on the dynamical status has been performed with the centroid shift parameter, which estimates the shift of the centroid of the X-ray isophotes and with the X-ray surface brightness concentration parameter, which takes into account the density peak in the innermost region of cool-core cluster. Concerning the first one, once the centroid of the largest aperture (or isophote), with a certain R_{max}, is obtained, the shift parameter is defined as follows:

$$w = \frac{1}{R_{max}} \sqrt{\frac{\sum \left(\Delta_i - < \Delta >\right)^2}{N - 1}}, \tag{3.10}$$

where Δ_i is the separation of the centroids computed within R_{max} and within the i^{th} aperture and N is the total number of aperture. The concentration parameter is defined as

$$c = \frac{S\,(r < 40 \text{ kpc})}{S\,(r > 400 \text{ kpc})}. \tag{3.11}$$

Here S is the X-ray surface brightness within a certain radius and this proxy is useful to recognize cool-core clusters, which have a density peak in the innermost region. For further informations on the cluster sample, we refer the reader to Vazza et al. (2017), Wittor et al. (2017), Angelinelli et al. (2020).

In Fig. 3.1 slices at z=0 of two clusters from our sample are shown. The upper panel shows the gas density and the lower panel the temperature distribution.

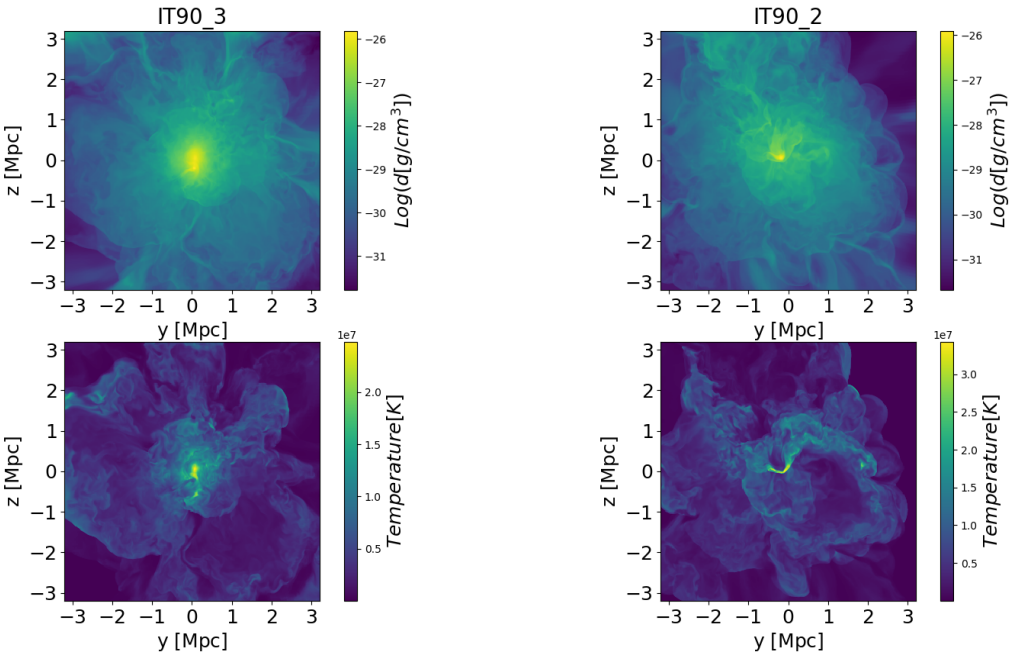

Figure 3.1: Gas density and temperature map of two cluster from the Itasca sample at z = 0.

4 Numerical analysis and results

In this section, we will present the numerical methods used to analyze the high-resolution outputs of a large sample of galaxy clusters, simulated with the cosmological adaptive mesh refinement code ENZO. We addressed the problem of relating the power spectrum of the velocity field of the ICM with gas density fluctuations, as commonly done in X-ray and SZ observations (e.g. Zhuravleva et al., 2014b). We compared these results with the radial profile of both density and velocity power spectra, and we investigated the relation between the slopes of the two spectra. Secondly, we also studied the role of buoyancy in the stratified ICM of galaxy clusters, and investigated whether the amplitude of gas density fluctuations across the cluster volume can be directly related with the Richardson number, following Mohapatra et al. (2020).

4.1 Radial profile of the power spectra

While a direct observation of turbulent motions via the Doppler effect on X-ray detectable emission lines is not yet feasible for the majority of galaxy clusters, the present sensitivity of X-ray satellites, combined with the proportionality of the surface brightness with the gas density, $S_X \propto n_{gas}^2$, makes it possible to infer, at least in principle, the amplitude of turbulent fluctuations through their impact on S_X. In order to compare the results with observational data, past analysis of simulations were restricted within the virial radius of the cluster. Moreover, the likely presence of shocks, clumps and filaments might contaminate the analysis. For this reason, both observationally and numerically, the properties of turbulence are typically difficult to constrain at large radii. As a preliminary step, we tried to understand how turbulence properties change, observing the radial profile of the power spectra of both density and velocity fluctuations. We measured the power spectrum of the velocity field of the simulated ICM using the Fast Fourier Transform, assuming periodicity (e.g. see Vazza et al., 2011, for a discussion) :

$$\mathbf{v}(\mathbf{k})^2 = \sqrt{v_x(\mathbf{k})^2 + v_y(\mathbf{k})^2 + v_z(\mathbf{k})^2}, \tag{4.1}$$

where $v_i(\mathbf{k})$ is the Fourier transform of each component

$$v_i(\mathbf{k}) = \frac{1}{(2\pi)^3} \int_V v_i(\mathbf{x}) e^{-2\pi i \mathbf{k}\cdot\mathbf{x}}\, d\mathbf{x}. \tag{4.2}$$

The density fluctuations $\rho(\mathbf{k})^2$ were obtained in a similar way, computing the Fourier transform of the real space density distribution. To obtain the power spectrum we did not disentangle turbulent from laminar fields, since the latter affects the bigger spatial scale, of the order of magnitude of the virial radius. In this sense, we carried on the analysis considering the region of the spectra in which there were no contaminations of both biggest spatial scales and smallest scales on which the turbulent dissipation becomes dominant. The chosen inertial range is $0.55 < Log(k) < 1.25$, where k is expressed in term of cells; in physical units this means a spatial scale L in the range 70 kpc $\lesssim$ L $\lesssim$ 350 kpc. In this sense, for example, Log(k) = 1 corresponds to a spatial scale L $\sim$ 200 kpc. Fig. 4.1 shows examples of the power spectra at various radii and the k range considered for the analysis, in the IT90_1 galaxy cluster, with $M_{200} = 2.45 \cdot 10^{14} M_\odot$ and $R_{200} = 1.29 Mpc$ (see Table 1). Finally, we evaluated the slope in each bin of the considered portion of the power spectrum and averaged them in order to obtain the slope mean for the entire power spectrum. Concerning the velocity power spectra, we evaluated the slope in each bin of each velocity component and then we averaged over all slope values within the considered range.

Firstly, in order to study the robustness of the method used for the estimation of the slopes and as a preliminary study of the dependence of the slopes on the radius, we investigated the dependence of the power spectra on the size of the computational box. The boxes are all centered on the peak of the gas density. We present the slope value as function of the size of the box, in a single cluster, in Fig 4.2. For each slope value, we give the one-sigma errorbar, evaluated as the standard deviation of the slope values

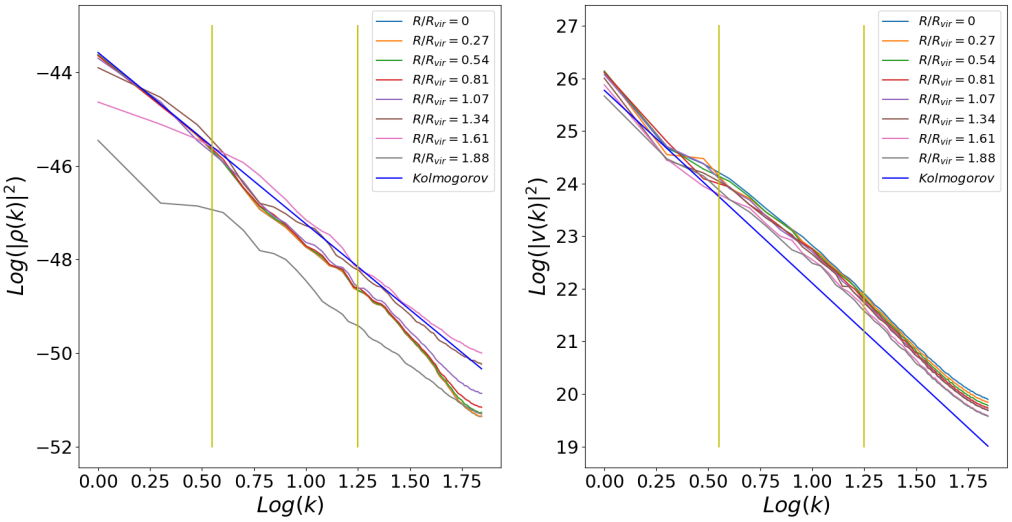

Figure 4.1: Power spectra of the density distribution (left panel) and velocity distribution (right panel) in IT90_1. The k values range used for the analysis is highlighted by the vertical yellow lines.

in each bin for both the density and velocity slope. The velocity slope is constant as the width of the box increases. On the other hand, even if the density slope becomes steeper, considering the errobars which make the slope values consistent each other, the profile suggests no variations as the size of the box increases. It is interesting to notice that Vazza et al. (2017), with the same cluster sample, found a steeper slope ($E(k) \propto k^{-4}$), considering larger boxes which include the whole volume of the galaxy cluster. On the contrary, in this work, we found a velocity slope which is consistent with a Kolmogorov scenario, whose prediction for the slope is -11/3 = -3.666 for a 3D spectrum. The explanation for this difference is likely to be that the normalization of the power spectrum decreases as we move to larger radii, resulting in a more steep spectrum if we consider a larger box than we used for this analysis. Therefore, this analysis highlights the important fact that a large dynamical range in simulations is necessary in order to properly measure the spectral slope of turbulent spectra, in an unbiased way with respect to numerical sampling effects.

In order to produce a slope radial profile, we computed the power spectra considering boxes with 128^3 cells located at different radii and in various directions, to fill the whole volume. The centre of the cluster was identified with the peak of the gas density. To have a unique slope value at a certain radius, we averaged the slopes, with an inverse-variance weighted mean, of the power spectra performed on boxes located at the same distance from the center of the galaxy cluster. Fig. 4.3 shows the slope radial profile in a cluster of our sample. Here, R_{vir} is the virial radius of the cluster. The one-sigma error-bars were estimated as the standard error of the weighted mean $\sigma = \left(\sqrt{\sum_i \frac{1}{\sigma_i^2}}\right)^{-1}$, where σ_i are the one-sigma errors of each box at a given radius. As above, the velocity slope shows a constant radial profile, whereas the density radial profile presents some variations. However, in the outer region, the presence of filaments and clumps, whose accretion might result in shocks, makes the explanation less straightforward. Despite this, both fields have a constant slope radial profile within R_{vir}, suggesting a rather stable relation between the density and velocity turbulent fluctuations.

In Fig. 4.4, 4.5, 4.6, 4.7, 4.8, 4.9, 4.10 we present the radial profile and the dependence on the size of the box of the slope for the other clusters. All of them show similar results as above, with a velocity slope similar to the Kolmogorov slope and a constant relation between the two slopes within the virial radius, as it might be widely expected if baryons would be a simple "passive" tracer advected by turbulent fluctuations. In the following sections, we will see that the relation between density and

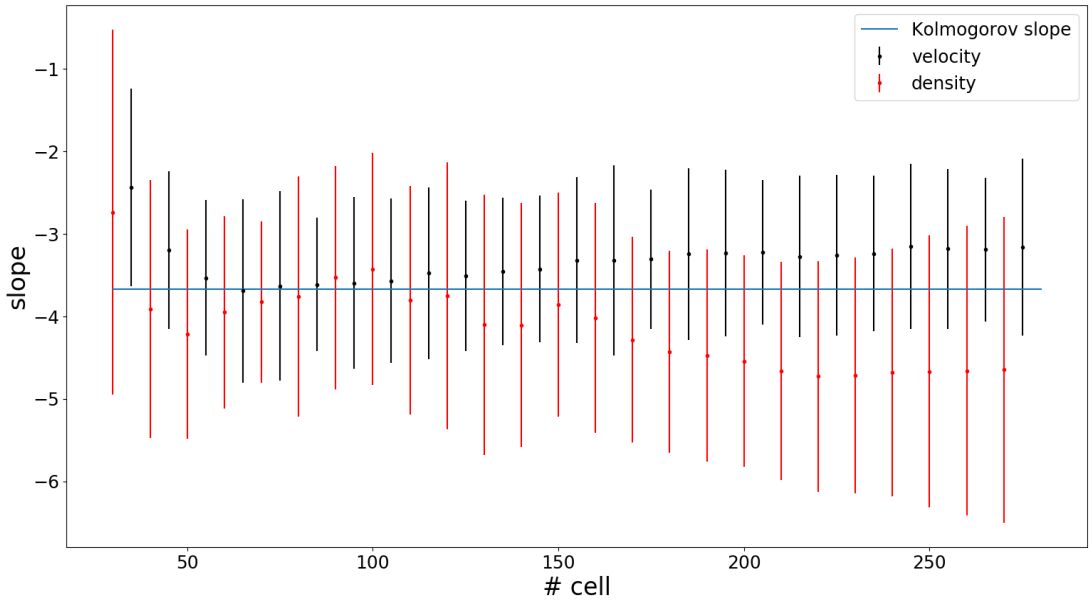

Figure 4.2: Power spectrum slope as a function of the width of the box. One-sigma error bars are shown. The velocity slope remains constant as the number of cells involved increases, whereas the density slope becomes steeper for box with cell number $> 200^3$.

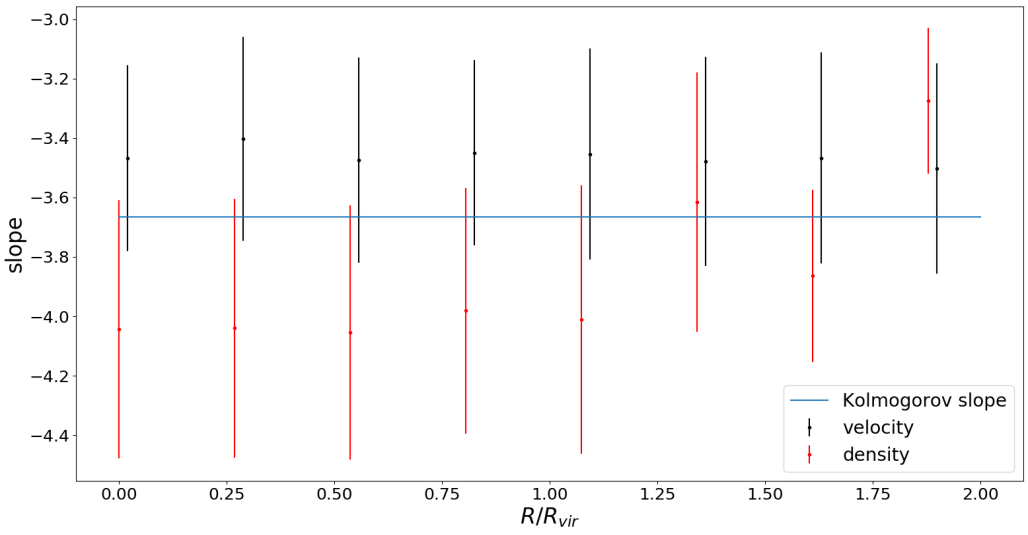

Figure 4.3: Power spectrum slope as a function of the distance from the cluster center. One-sigma error bars are shown. The velocity slope remains constant as we move to larger radii, whereas the density slope becomes flatter.

velocity fluctuations is indeed more complex in the typical environment of galaxy clusters.

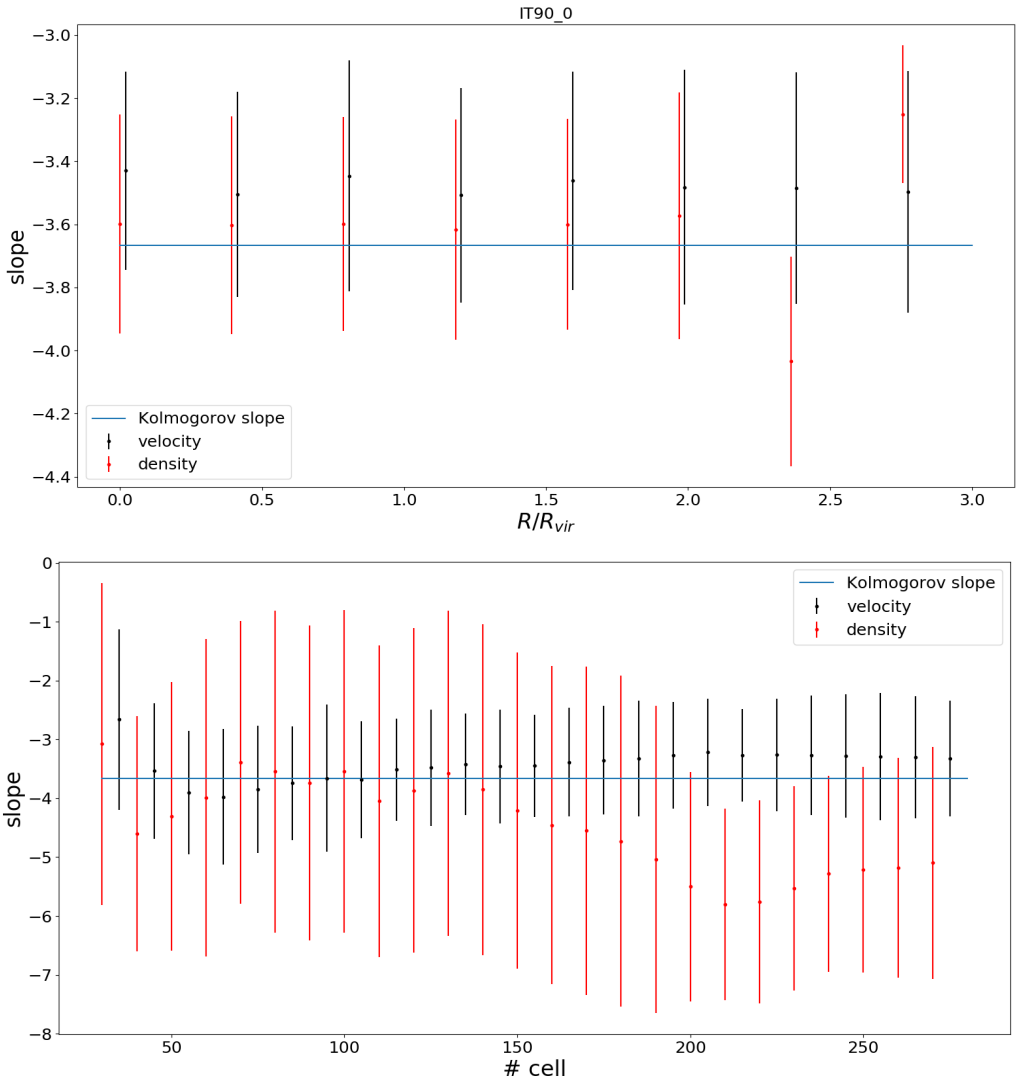

Figure 4.4: Power spectrum slope as a function of the distance from the cluster centre (top panel) and the width of the box (low panel) in IT90_0

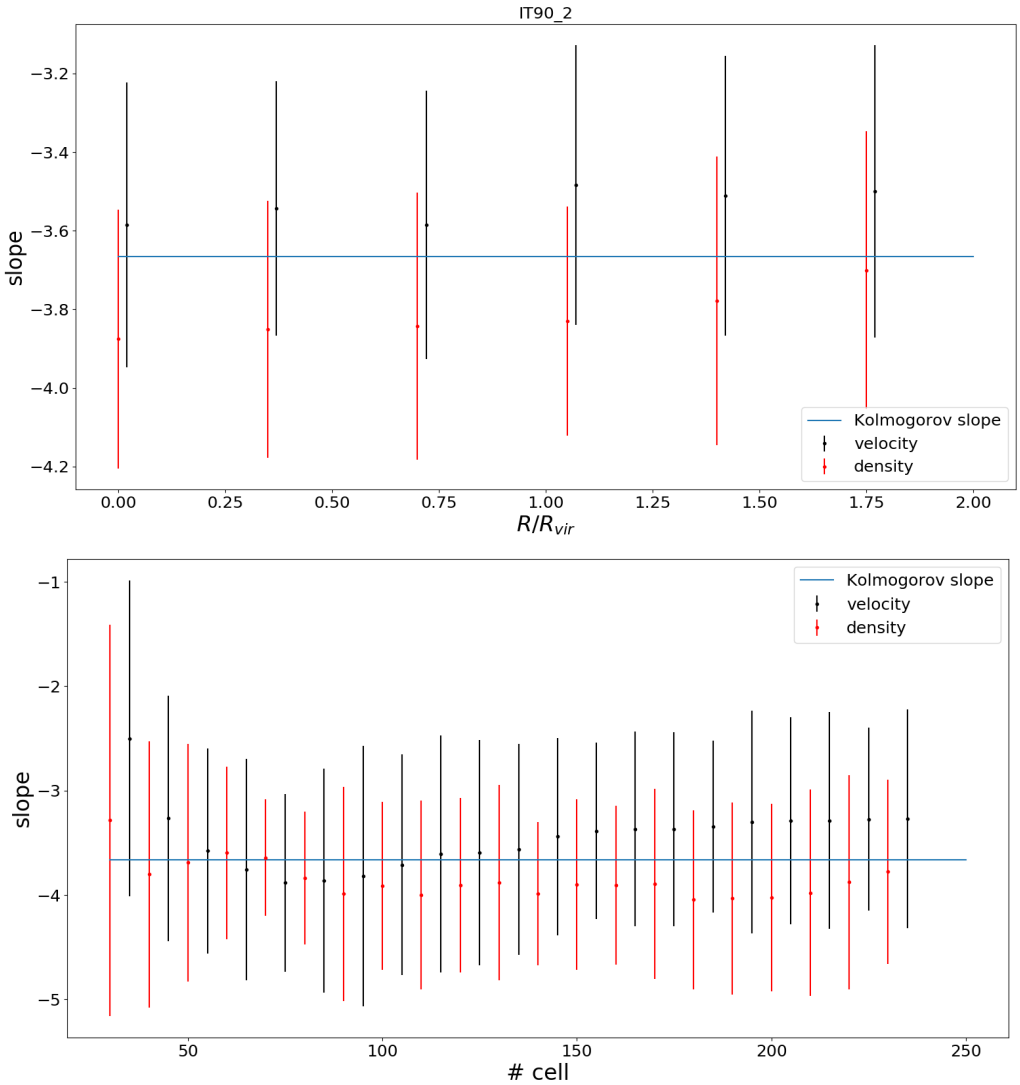

Figure 4.5: Power spectrum slope as a function of the distance from the cluster centre (top panel) and the width of the box (low panel) in IT90_2

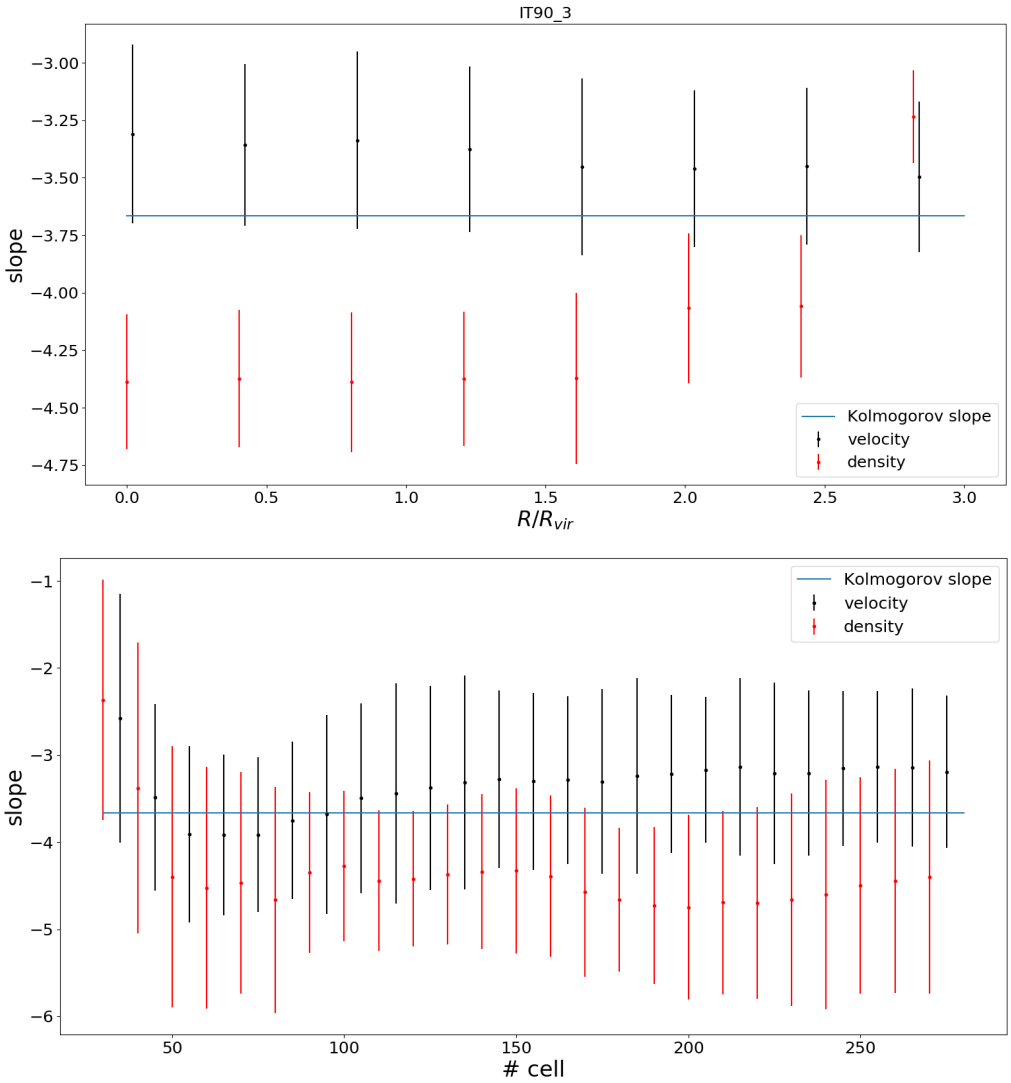

Figure 4.6: Power spectrum slope as a function of the distance from the cluster centre (top panel) and the width of the box (low panel) in IT90_3

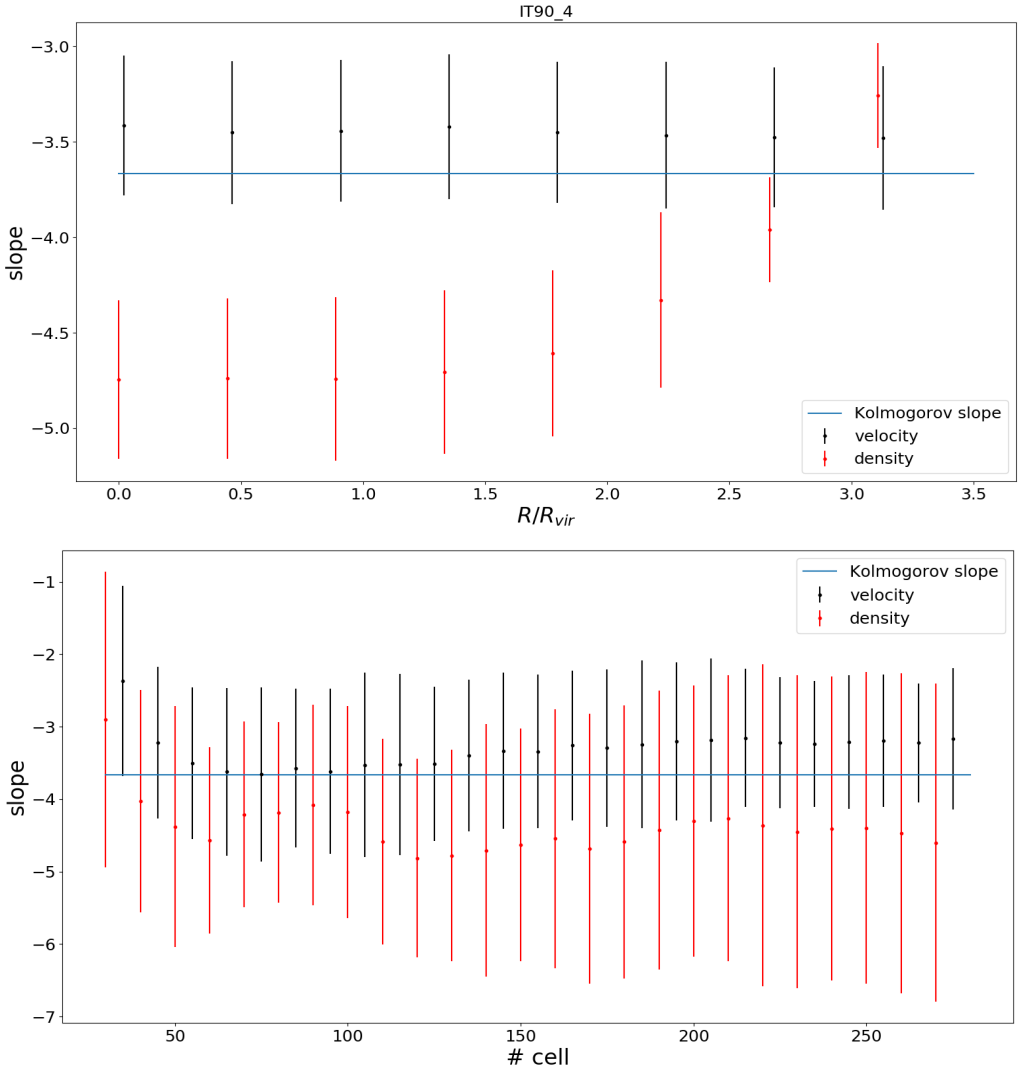

Figure 4.7: Power spectrum slope as a function of the distance from the cluster centre (top panel) and the width of the box (low panel) in IT90_4

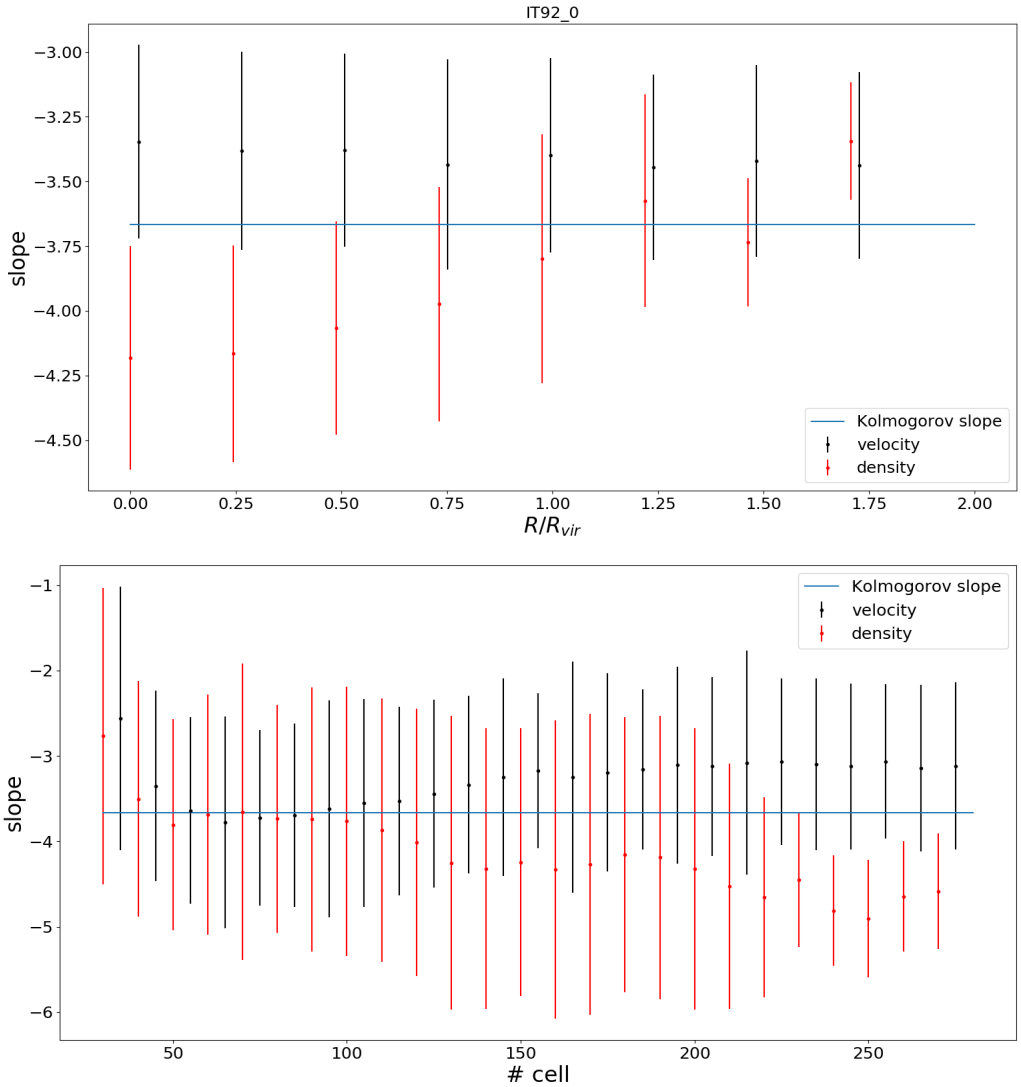

Figure 4.8: Power spectrum slope as a function of the distance from the cluster centre (top panel) and the width of the box (low panel) in IT92_0

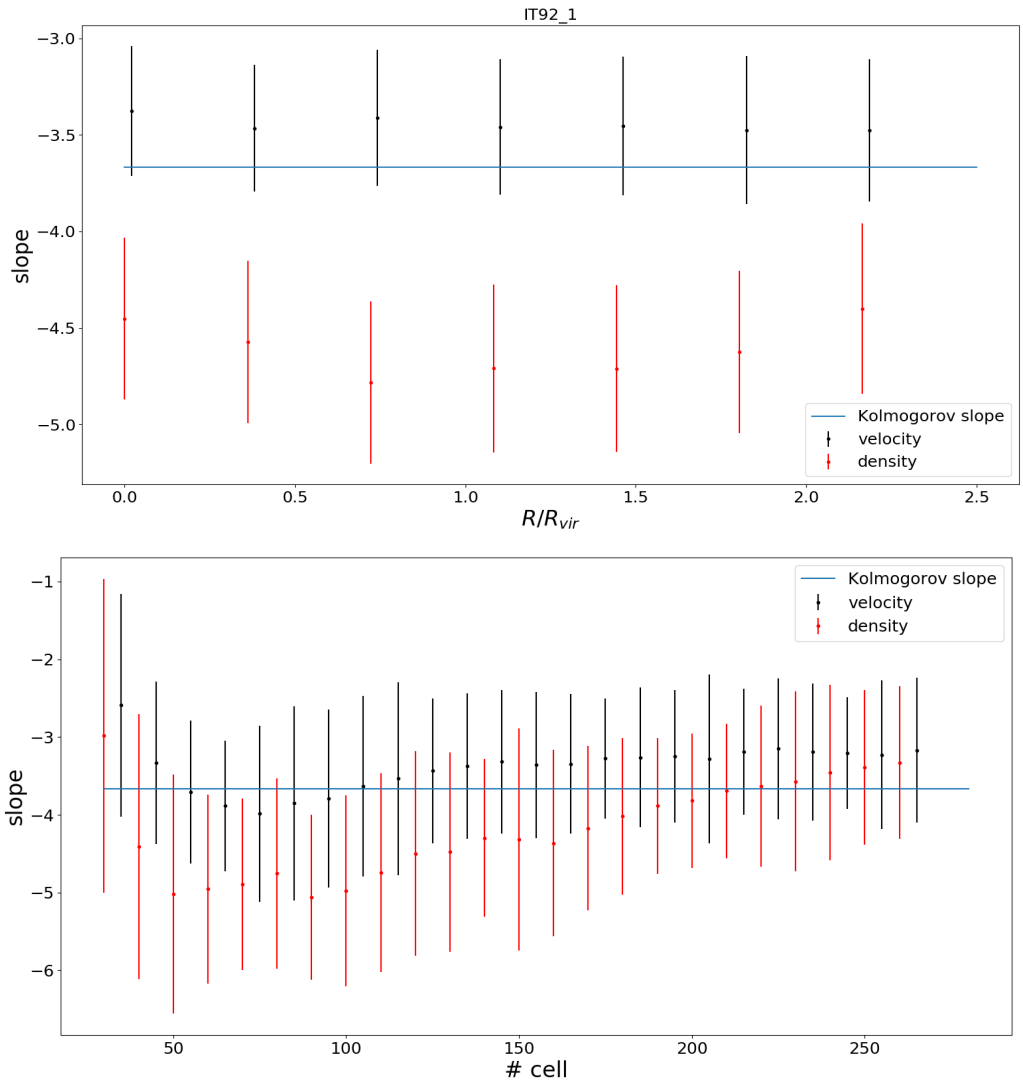

Figure 4.9: Power spectrum slope as a function of the distance from the cluster centre (top panel) and the width of the box (low panel) in IT92_1

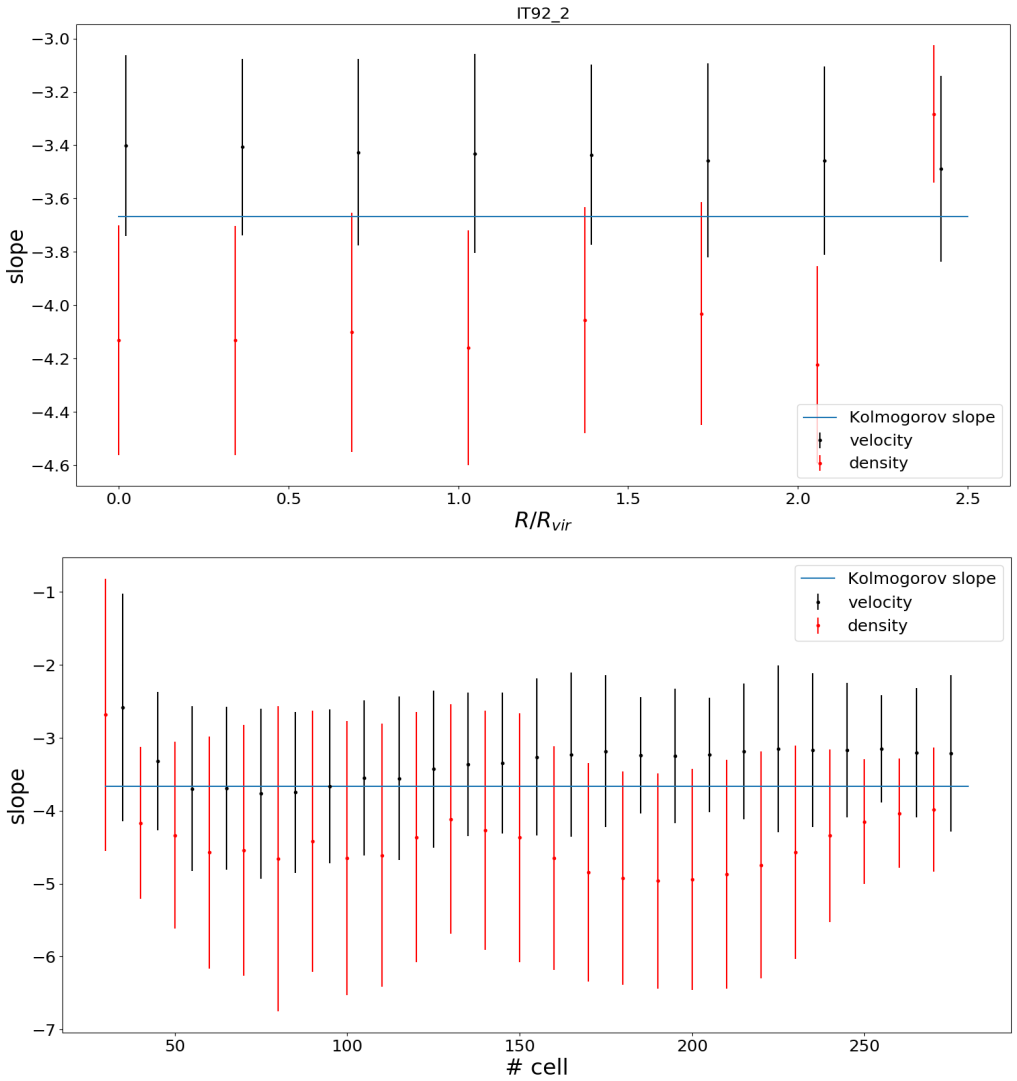

Figure 4.10: Power spectrum slope as a function of the distance from the cluster centre (top panel) and the width of the box (low panel) in IT92_2

4.2 On the relation between velocity and density turbulent fluctuations

The easiest observational approach to infer information on the turbulent velocity fluctuations in X-ray band, is the study of the surface brightness fluctuations, supposing that they are related to density fluctuations produced by turbulent motions. Zhuravleva et al. (2014b) and Gaspari et al. (2014) studied the $\delta\rho/\rho - \delta v/c_s$ relation in the stratified intracluster medium. In the first work, the authors performed a cosmological simulation to analyze the merger-driven turbulence in 6 relaxed clusters. On the other hand, in the latter work, the authors investigated the turbulent statistics in more idealised simulations. Both of them found that the rms of density and velocity fluctuations are linearly related, across a broad range of scales, in both buoyancy-dominated and turbulent regimes.
We extended the analysis, studying the above relation in both relaxed and perturbed galaxy clusters in the ITASCA sample (Sec. 3.2). In order to study the properties of turbulence, it is useful to disentangle the bulk and turbulent motions. Different algorithms have been performed and there is no consense on the

best approach. For this reason, we implemented different methods to observe how the $\delta\rho/\rho - \delta v/c_s$ relation changes as different algorithms are considered. In particular, we estimated the turbulent fluctuations in the following ways:

- $\delta\rho(prof) = \frac{\rho - \bar{\rho}_{prof}}{\bar{\rho}_{prof}}$. Here $\bar{\rho}_{prof}$ is the density mean, at a certain radius, given by the 3D radial profile. The variance of this variable is called $\sigma^2_\rho(prof)$.
- $\delta\rho = \frac{\rho - \bar{\rho}}{\bar{\rho}}$, where $\bar{\rho}$ is the density mean evaluated on 300 kpc wide boxes. This is a scale-filtering approach with a 300 kpc fixed scale. The top-right panel of Fig. 4.11 shows the density distribution after the procedure to disentagle the bulk motions using this method. The variance of this variable is called σ^2_ρ.
- $\delta v_i(prof) = \frac{v_i - \bar{v}_{iprof}}{cs_{prof}}$. We computed the 3D radial profile for each velocity component v_{iprof} and we estimated $\delta v(prof) = \sqrt{\delta v_x^2 + \delta v_y^2 + \delta v_z^2}$. The sound speed at a given radius, cs_{prof}, was evaluated from the temperature 3D radial profile, using Eq. 4.6. Its varaince is $\sigma^2_v(prof)$.
- $\delta v_i = \frac{v_i - \bar{v}_i}{cs_{prof}}$, where $\bar{v}_i$ is the density-weighted velocity mean of the i-th component evaluated on 300 kpc wide boxes . The method is analogous to the fixed-scale filtering approach for the density distribution. Lower-right panel of Fig 4.11 shows the residual turbulent motions. We calculated the modulus δ_v as before. We will refer to the variance of this variable as σ^2_v.

Since we studied turbulence injected from hierarchical accretion, it is likely that, if there are motions on large scale, they are related to bulk motions of the gas. Moreover, Angelinelli et al. (2020), with an iterative multi-scale filtering approach (in the same clusters sample) found that the most likely scale is about 500 kpc. For these reasons, we are confident the filtering scale chosen value might be reasonable.

The analysis was computed within the virial radius of the clusters and, in order to study the whole considered volume, we analyzed, with the following algorithm, $\approx$ 600 kpc (linear size) wide boxes (with 32^3 cells), located at different radii and considering various radial directions. In each box we computed the probability distribution function (PDF) of the density turbulent fluctuations (Fig. 4.12, orange plus blue line). In order to remove the contaminations coming from shock compressions and accreted sub-halos, we excised the 5% denser cells in each box considered. The orange line in Fig. 4.12 shows the resulting PDF after this procedure. The density fluctuation σ^2_ρ (σ^2_ρ(prof)) in each box was estimated as the variance of the includes points of the PDF. Similarly, the velocity fluctuation σ^2_v ($\sigma^2_{\rm v}$(prof)) was calculated as the variance of the velocity in each cell in which the density fluctuation was in the range of $\delta\rho/\rho$ values included in the PDF after the removal of the denser fluctuations.

As it is shown in Fig. 4.13, the two methods to infer the velocity fluctuations give quite different results, but, for small values, it is reasonable to think that the small differences might not affect the final result. In the plot, there are the values of the turbulent velocity fluctuations evaluated with two different methods (black points) and the y=x line (red line). The last method presented in the above list is supposed to be more accurate, since the velocity mean is estimated locally, around the cell to filter. For this reason, we used the results from this method to fit the data. On the other hand, the density fluctuations, estimated with the two different methods above, deviate between one to the other. In particular, in the case in which $\bar{\rho}$ is estimated from the radial profile, very large fluctuations ($\sigma^2_\rho(prof) > 10$) appear, even with the cut of the 5% denser fluctuations. A possible explanation for these findings is that this method is insufficient to filter the largest accreted structures. Moreover, a radial mean does not takes into account the presence of a clump, resulting in large local fluctuations.
In this latter case, the linear fit is unstable both for relaxed and perturbed cluster, resulting in a nearly costant relation: $m = 0.02 \pm 1.17 \cdot 10^{-4}$, $R = 9.7 \cdot 10^{-4}$ and $7.7 \pm 1.3 \cdot 10^{-3}$, $R = 0.39$ for the perturbed and relaxed clusters (according to the centroid shift parameter), respectively. For completeness, we report the fit of this case in Fig. 4.14. Since the number of points with $\sigma^2_\rho > 10$ is small, the figure has limits

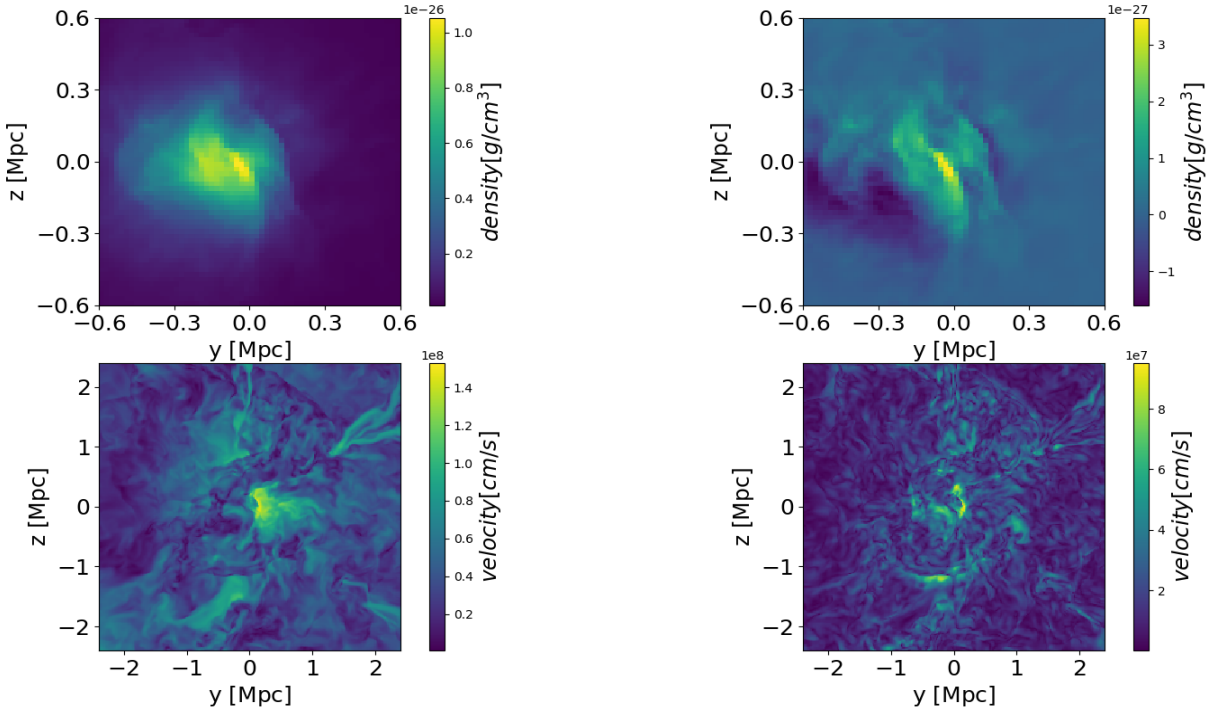

Figure 4.11: In the left panels, the original density and velocity distributions in one cluster. In the right panels, the turbulent density and velocity fluctuations after the application of the fixed-scale filtering method.

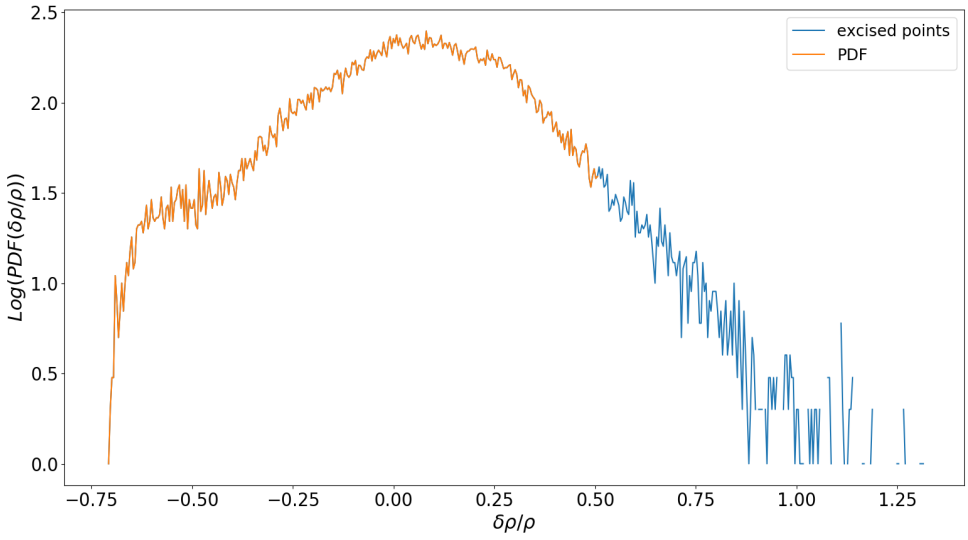

Figure 4.12: Probability distribution function of the turbulent density fluctuations in a single box of a cluster. The orange points are the final PDF, after the procedure to excise the 5% denser fluctuations. The blue part represents the excised points.

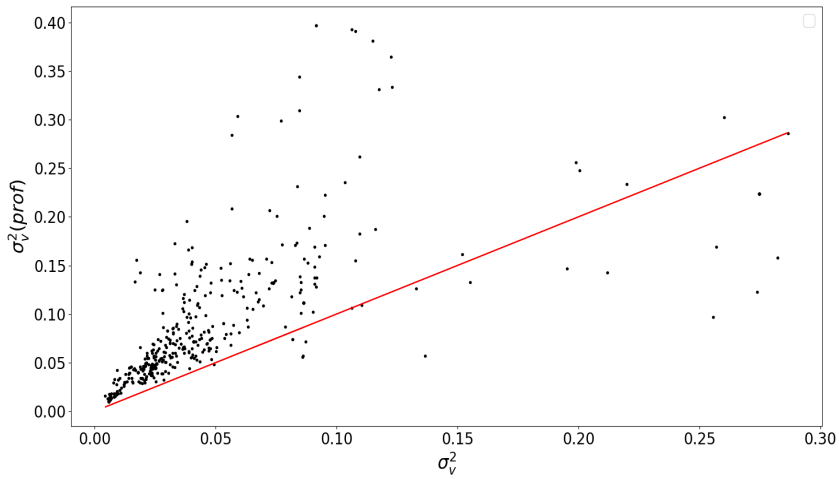

Figure 4.13: σ_v^2 - $\sigma_v^2(prof)$ plot. The red line is the bisector y=x. At small values the two methods give quite similar results.

on x-axis for a better visualization. To test the goodness of the fit we used the Pearson's correlation coefficient

$$R = \frac{\sum_i (x_i - \bar{x})(y_i - \bar{y})}{\sqrt{\sum_i (x_i - \bar{x})^2 \sum_i (y_i - \bar{y})^2}}, \tag{4.3}$$

where $\bar{x}$ and $\bar{y}$ are the means of the two variables. This parameter is equal to 1 (-1) when the variables are perfectly correlated (anti-correlated), while is zero when the variables are completely uncorrelated.

On the contrary, considering the density fluctuations with $\bar{\rho}$ evaluated on boxes, the results show a significant relation between the two variables. In Table 2 the parameters of the fit with the classification of the dynamical state of the clusters, based on the centroid shift parameter, are reported, while in Fig. 4.15 we show the fit. R is the Pearson's correlation coefficient, m is the slope and q is the intercept.
In Table 3 we report the fit parameters, classifying the dynamical state of the galaxy clusters according to the value of the X-ray surface brightness concentration (Table 1). Fig. 4.16 shows that, in this case, the relation remains for the perturbed clusters but disappears for the relaxed clusters. However, the number of relaxed clusters is small, in particular with the classification based on the concentration parameter. In this sense, the fit is likely to be affected by small number statistics and some variations might arise if we consider a larger sample. Moreover, since the concentration parameter is the ratio between the flux in the innermost region and the "total" flux of the cluster, it is used to recognize the cool-core clusters, which usually are relaxed. On the other hand, the simulations performed are non-radiative, which means that the classification based on the concentration parameter might be less accurate than the classification according to the centroid shift, because some of the relevant physics responsible for the production of cool-cores (e.g. radiative cooling, star formation and feedback) is just missing in the numerical model.

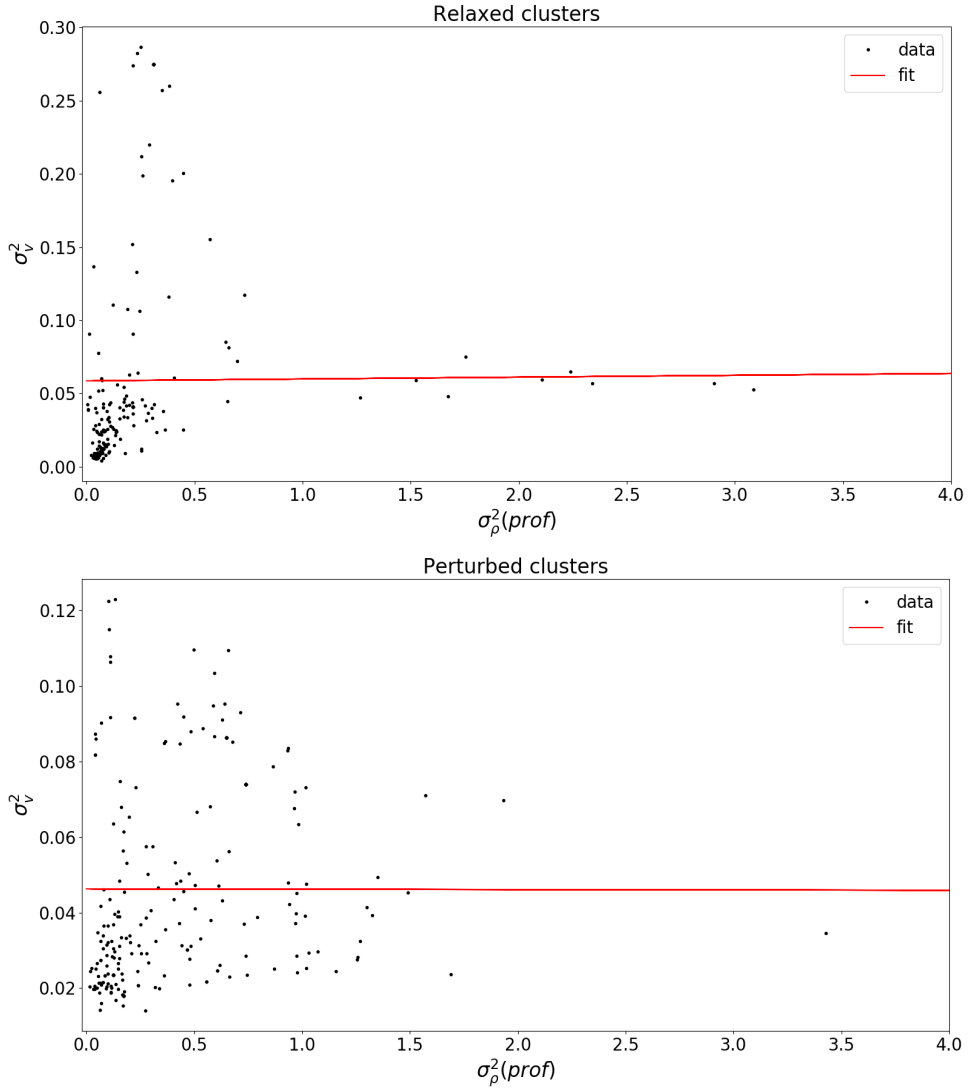

Figure 4.14: σ_ρ^2 - σ_v^2 plot in relaxed (upper panel) and perturbed (lower panel) galaxy clusters. The density mean is evaluated from the 3D radial profile.

	R	m	q
Total cluster sample	0.58	0.59 ± 0.04	-0.015 ± 0.005
Perturbed clusters	0.45	0.27 ± 0.03	0.011 ± 0.005
Relaxed clusters	0.77	0.99 ± 0.06	-0.038 ± 0.007

Table 2: Parameters of the linear fit between linear density and velocity turbulent fluctuations. The density and velocity mean are evaluated on 300 kpc wide boxes. The cluster dynamical state classification is based on the centroid shift parameter w.

	R	m	q
Perturbed clusters	0.64	0.68 ± 0.04	0.020 ± 0.005
Relaxed clusters	-0.05	-0.017 ± 0.036	0.033 ± 0.004

Table 3: Parameters of the linear fit between linear density and velocity turbulent fluctuations. The density and velocity mean are evaluated on 300 kpc wide boxes The cluster dynamical state classification is based on the X-ray surface brightness concentration c.

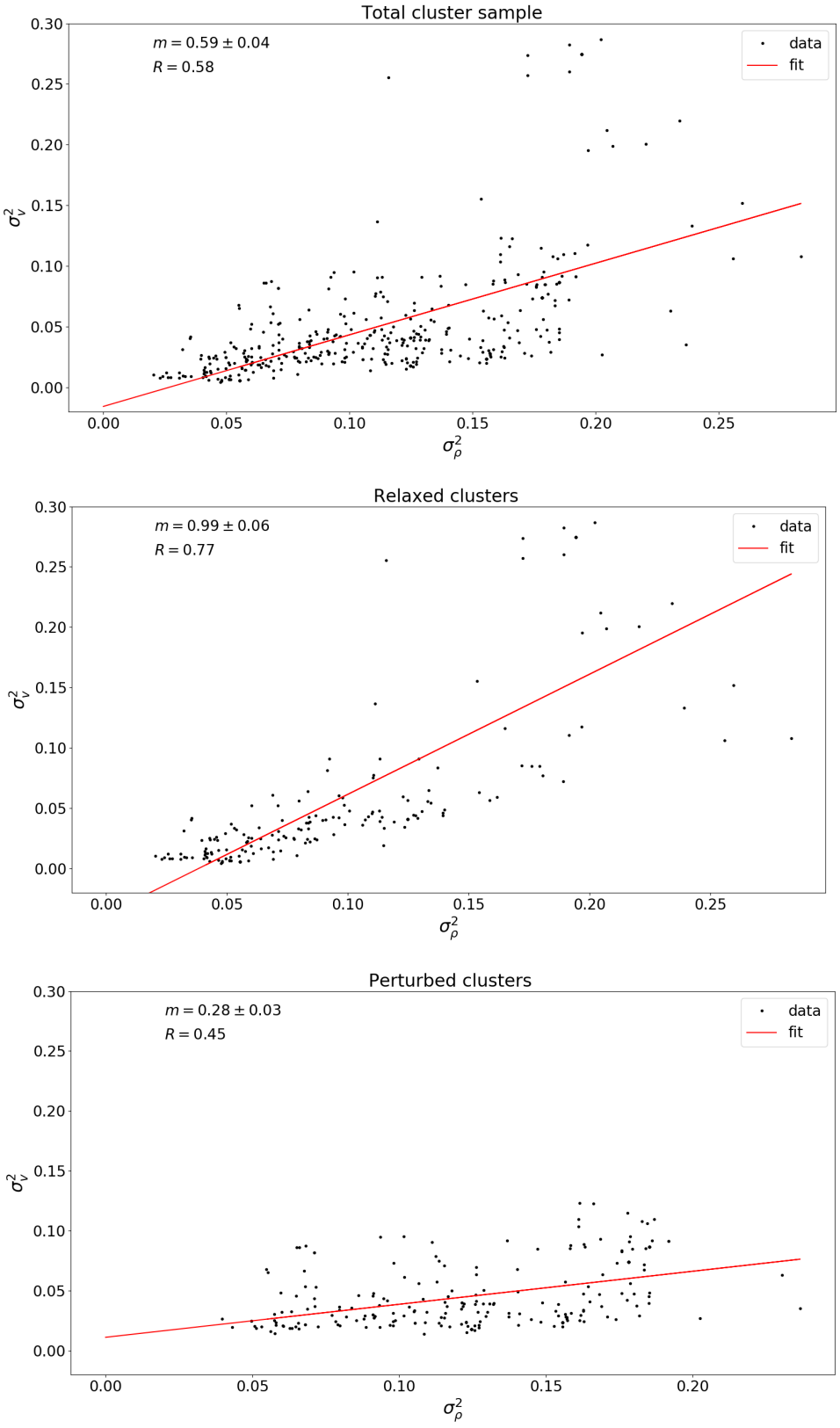

Figure 4.15: σ_ρ^2 - σ_v^2 plot in the total cluster sample (upper panel), in the relaxed (middle panel) and perturbed (lower panel) galaxy clusters. The density and velocity mean are evaluated on 300 kpc wide boxes. The cluster classification is based on the centroid shift parameter.

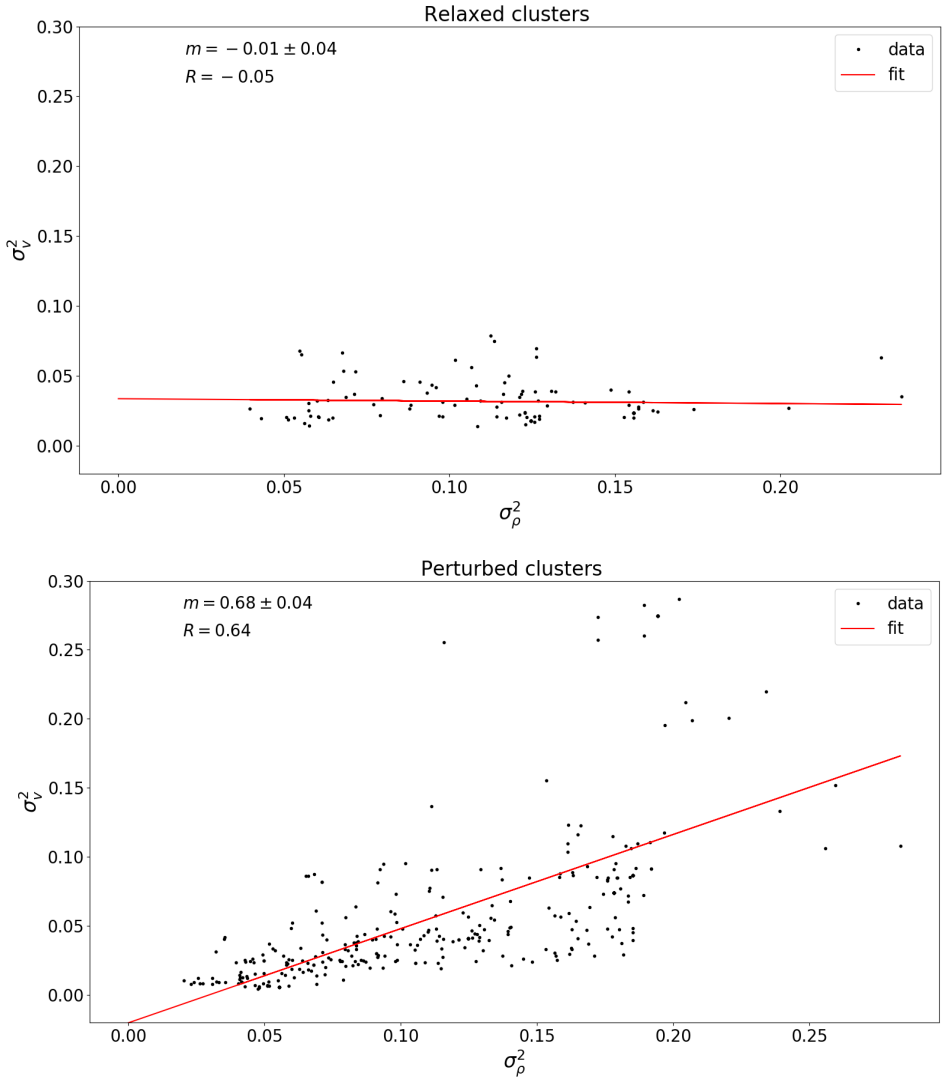

Figure 4.16: σ_ρ^2 - σ_v^2 scatter plot in relaxed (upper panel) and perturbed (lower panel) galaxy clusters. The density mean is evaluated on 300 kpc wide boxes. The cluster classification is based on the X-ray surface brightness concentration.

4.3 Testing the $R_i - \mathcal{M} - \sigma_s^2$ relation

Mohapatra et al. (2020) studied the role of the stratification in a turbulent plasma, showing that density fluctuations generated in this scenario depend on the Richardson number, which takes into account the stratification, and the Mach number. We tested the validity of the picture presented in the previous work in a more complex and time dependent plasma. The considered clusters region is within the virial radius and we implemented the following algorithm on boxes with 32^3 cells, located at different radii and considering various radial directions. We used the peak of gas density distribution to recognize the center of the cluster.
To disentangle the bulk and turbulent motions we used the fixed-scale filtering approach presented above. For unstratified subsonic turbulence, the density fluctuations are supposed to follow a log-normal distribution (Federrath et al. 2008, Zhuravleva et al. 2013). For this reason, and to follow the reference work, we used logarithmic density fluctuations for our analysis:

$$s = ln\left(\rho/\bar{\rho}\right), \tag{4.4}$$

where ρ is the original field and $\bar{\rho}$ is the density mean evaluated on 300 kpc wide boxes around the cell to filter. The resulting probability distribution function of density fluctuations is presented in Fig. 4.17 (blue line plus orange line). It was obtained in one of our clusters, considering a region of 32^3 cells ($\approx$ 600 kpc linear size wide box). The distribution has two tails both at smallest and largest values of s which make it different from a log-normal distribution. Anyway, as discussed above, high s values are expected, as shock compressions and accreted filaments are present in galaxy clusters. For this reason, as in the previous analysis, we excised the 5% denser fluctuations in each box considered. The resulting PDF, after this procedure, is presented in Fig 4.17 (orange line). The density fluctuation σ_s^2 in each box was estimated as the variance of the includes points of the PDF.

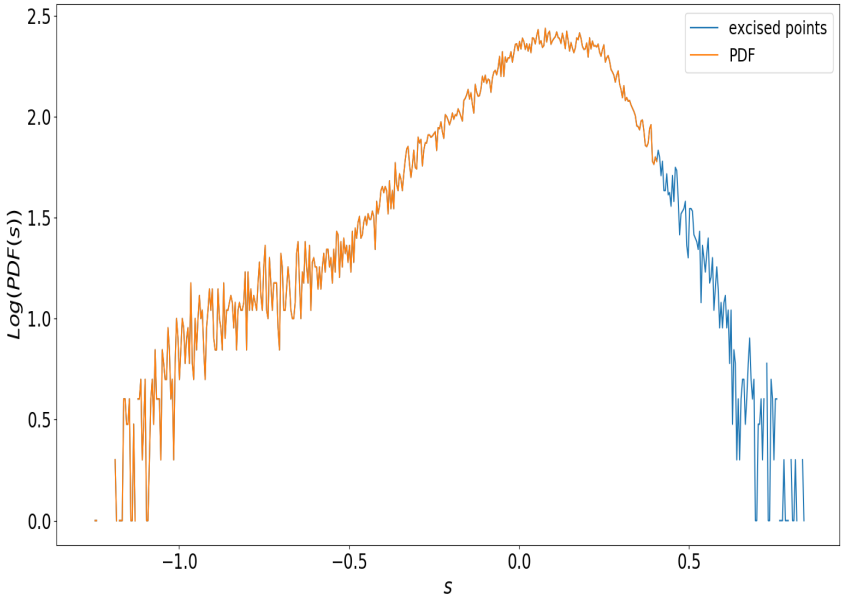

Figure 4.17: Probability distribution function of the logarithmic density fluctuations in a box of a cluster. The orange points are the final PDF, after the procedure to excise the 5% denser fluctuation. The blue part represnts the esxcised points.

To estimate the Richardson number we used the Eq. 2.33. We divided each box of 32^3 cells with 30 shells to create the radial profiles. The Brünt-Väisälä frequency was evaluated following the Eq. 2.32 computing a centered derivative. Tha gas pressure and density are given by the radial profile in the box

as the gravitational acceleration, which we computed, considering a spherical symmetry, making use of the Newton's theorem

$$g(r) = -\frac{GM(r)}{r^2}. \tag{4.5}$$

Here, M(r) is the total mass of the cluster ($M_{gas} + M_{DM}$) at a given radius. The adiabatic index γ is 5/3. We derived the turbulent velocity radial profile, within the box, and the value of v_l in each shell was estimated as the quadratic mean of the turbulent velocities of each cell, belonging to the shell, in which the density fluctuation was in the range of s values included in the PDF after the cut of the denser fluctuations. Furthermore, we assumed the filtering scale l as the dimension of the boxes on which we filter the density and velocity distribution, $l = 300$ kpc. Once R_i was evaluated in each shell, we averaged it, in order to characterize each box with its Richardson number.

Finally, we evaluated the Mach number mean averaging the Mach number ($\mathcal{M} = v_l/c_s$) of each cell belonging to the box. The sound speed in each cell was derived from the temperature

$$c_s = \sqrt{\gamma \frac{kT}{\mu m_p}}. \tag{4.6}$$

Fig. 4.20 shows a distribution of the Mach number considering the total cluster sample. We plot the $\sigma_s^2 - R_i$ relation in Fig. 4.18. The relation we found is clearly different from the fit founded by Mohapatra et al. In the plot the black points are the results of the analysis, while the blue line is the best fit found by Mohapatra et al; the density fluctuations we found are larger than the σ_s^2 values found in the reference work.

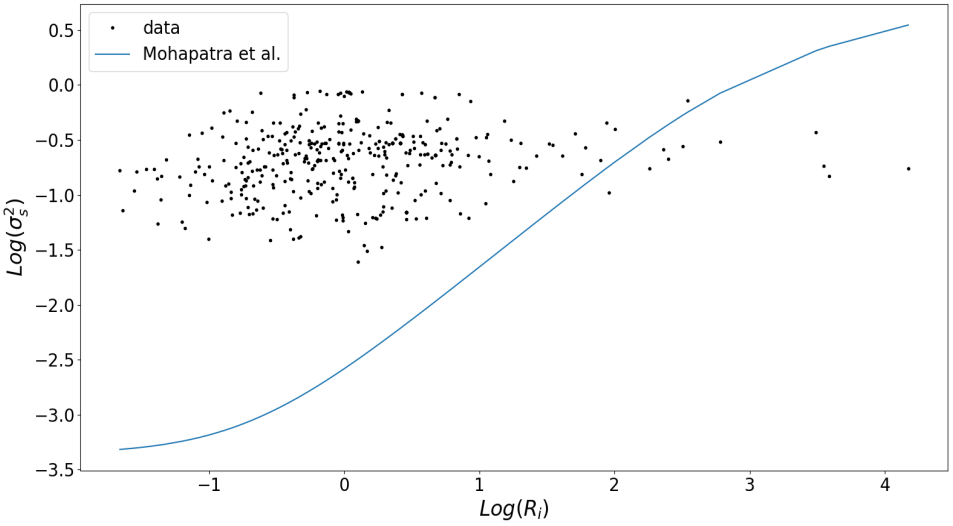

Figure 4.18: R_i - σ_s^2 plot. Both variables are calculated on box with 32^3 cells located at different radii. The analysis was performed considering the total cluster sample

In order to explore the balance between turbulence and buoyancy as function of the radius, we also computed a radial profile of the Richardson number, repeating the same steps above in a larger box which includes the cluster region beyond the virial radius. Fig 4.19 gives the different radial profile of R_i , for boxes of increasing size. We found that the Richardson number has a strong dependence on the filtering scale, with the possibility of varying of almost two orders of magnitude going from the smallest to largest filtering scales. According to the Kolmogorov theory, $R_i \propto l^{4/3}$, but the plot shows how the Richardson

number has a steeper rise. For L $\leq$ 100 kpc, R_i is always smaller than one, suggesting that buoyancy is inefficient and the property of homogeneity and isotropy of the turbulence probably still be present. On the other hand, For L $\geq$ 300 kpc buoyancy seems to be dominant for most of the volume of the cluster. Only in the more peripheral regions, turbulence takes over the gravity. Finally, the radial profile does not change its shape, suggesting that the turbulent velocity radial profile does not change increasing the filtering scale. This is in agreement with the results presented in Fig. 4.2, which shows that the velocity slope does not change as the size of the box (analogous to the filtering scale) increases.

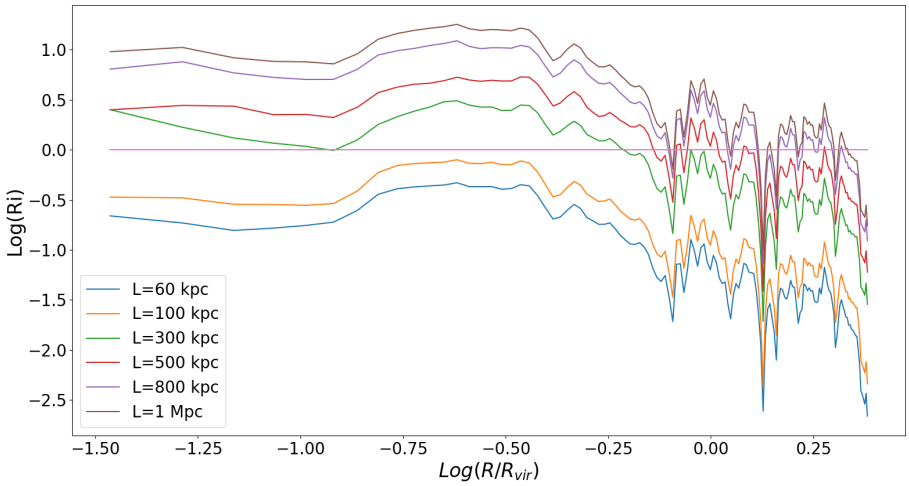

Figure 4.19: Richardson number radial profile for a single cluster. Different colors mean different filtering scales (L), evaluated as the dimension of boxes in which the velocity mean of laminar flow is estimated. Magenta line traces when Ri=1.

For a more complete study of the density fluctuations dependence on the Richardson number, we also tested the $R_i - \mathcal{M} - \sigma_s^2$ relation considering the Richardson number and s = $ln(\rho/\bar{\rho})$ evaluated on shells at different radii. We divided the entire cluster with 250 shells and, in each of them, we estimated σ_s^2 as the variance of the PDF after the procedure to excise the denser fluctuations. In Fig. 4.21 we present the $R_i - \sigma_s^2$ scatter plot for this case. In this case, the relation is different from the reference work as well. Besides, we are confident that the method explained above is more accurate. In fact, a radial mean cancels possible asymmetries and both the Richardson number and σ_ρ^2 show different values as the direction, in which the box is located, changes, even at the same radius. In conclusion, we assessed that an analysis of turbulence has to be performed on boxes, since the turbulent properties are affected by the asymmetry of the system and sphericity assumption.
Anyway, both using boxes or radial profile, we found strongly different results from Mohapatra et al. In particular, the logarithmic density fluctuations we obtained for small Richardson number are larger up to 3 order of magnitude. This might be caused by the different nature of the simulations (idealised and cosmological). Since small Richardson number results in turbulence dominated regime, the different turbulent forcing in the two simulations might result in different density fluctuations. Moreover, as Fig. 4.19 shows, we found small Richardson numbers in the outer region of the cluster, in which shocks and accretion processes might contaminate the results. In this sense, even if the average Mach numbers we found on each box suggest subsonic turbulence (see Fig. 4.20), this does not mean that locally the gas is not in a supersonic regime. On the other hand, Mohapatra et al. investigated turbulence in a subsonic regime. This might also explain the logarithmic density PDF we obtained. Federrath et al. (2008) showed how compressive supersonic turbulence results in a PDF with a higher tail at the smallest values, which is very similar to the PDF we obtained (Fig 4.17). Since the distribution we obtained is clearly not log-normal, estimating the density fluctuations using the variance might not be the best approach and some other way must be investigated.

	R	m	q
Total cluster sample	0.12	0.04 ± 0.02	0.12 ± 0.01
Perturbed clusters	0.19	0.12 ± 0.04	0.09 ± 0.01
Relaxed clusters	0.11	0.02 ± 0.02	0.14 ± 0.01

Table 4: Parameters of the linear fit between logarithmic density and velocity turbulent fluctuations.

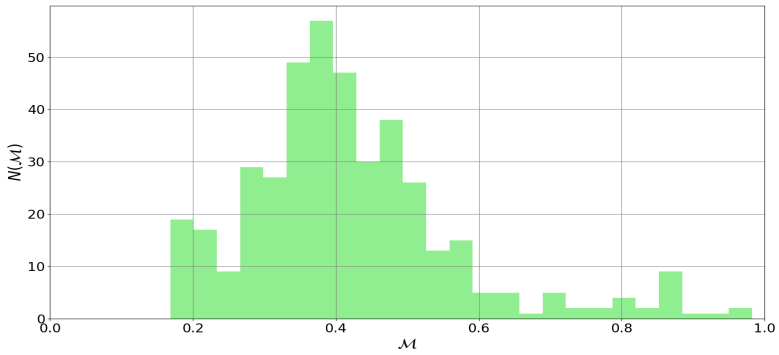

Figure 4.20: Distribution of the Mach number estimated averaging the Mach number of each cells belonging to a certain 600 kpc (linear size) wide box.

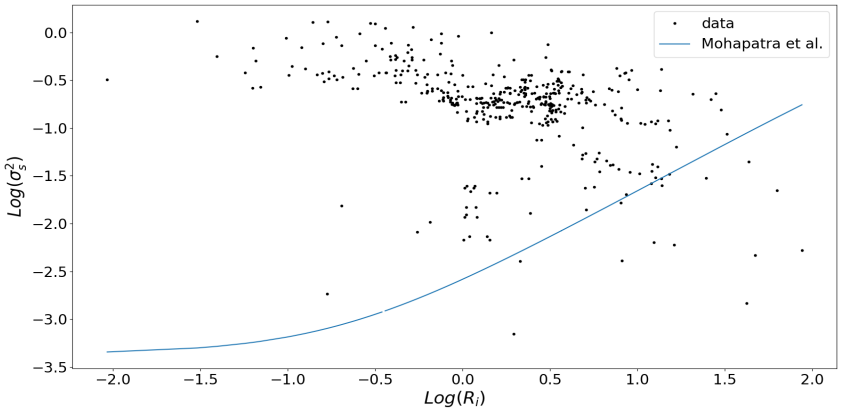

Figure 4.21: R_i - σ_s^2 scatter plot. Both variables are calculated on shells at different radii. The analysis was performed considering the total cluster sample.

Finally, we investigated the relation between the logarithmic density and velocity ($ln(v/\bar{v})$) fluctuations. We performed a linear fit between the two variables, considering the whole sample and differentiating between perturbed and relaxed clusters. In all these cases we found no dependence (i.e. slope m consistent with zero). In Table 4 are reported the parameters of the fit and in Fig. 4.22 we show the fit. Only the perturbed clusters show a relation between the logarithmic fluctuations, but with a large scatter which results in a small correlation coefficient.

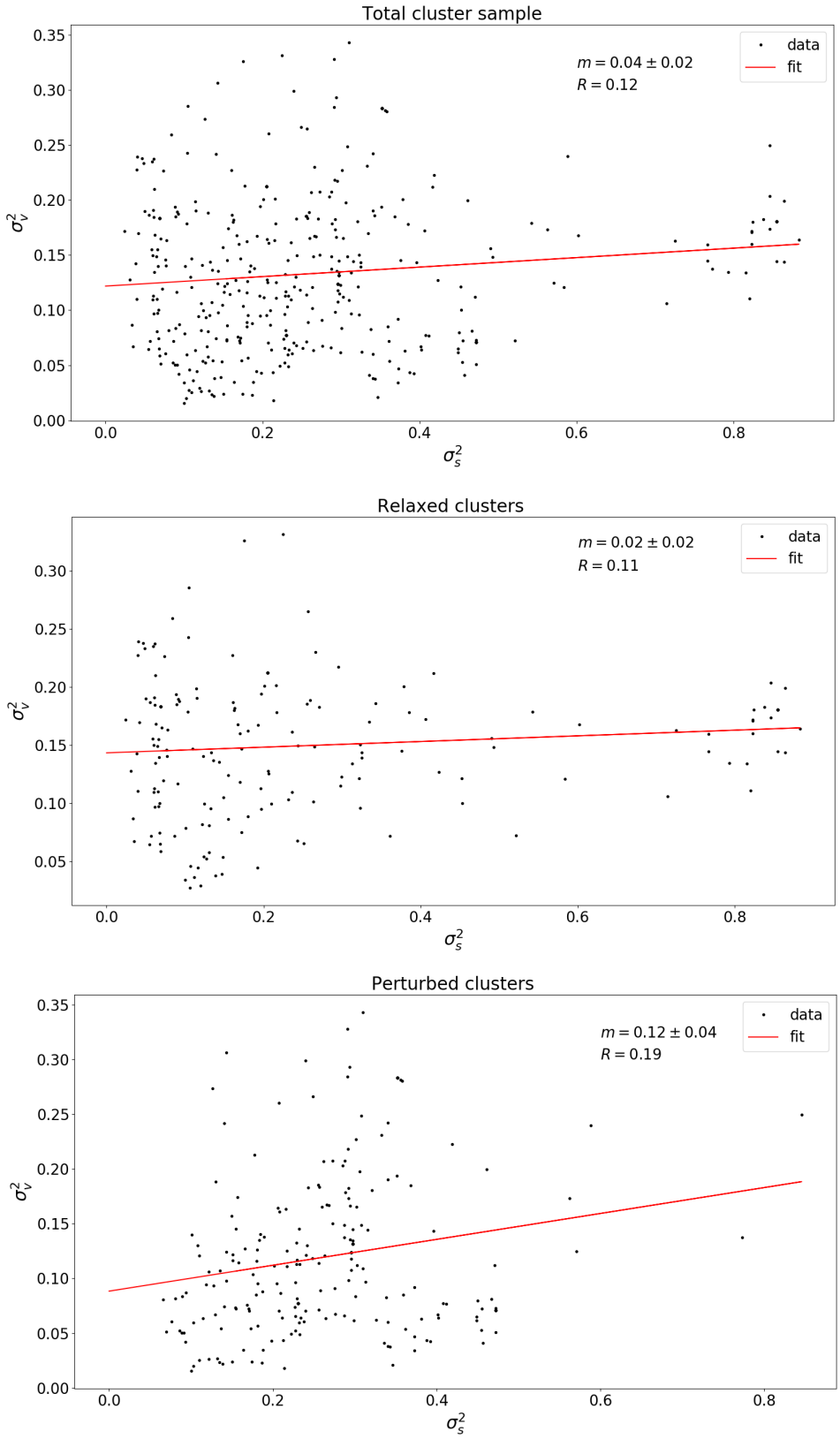

Figure 4.22: $\sigma_s^2 - \sigma_v^2$ relation, considering logarithmic fluctuations, in the total cluster sample (upper panel), relaxed clusters (middle panel) and perturbed clusters (lower panel). Both density and velocity mean are evaluated in 300 kpc wide boxes.

5 Comparison with the literature and future developments

In this work, we analyzed a sample of galaxy clusters, simulated with the cosmological code ENZO, in order to investigate the statistical properties of turbulence arising from hierarchical accretion process. We studied the radial dependence of the slope of, both, density and velocity power spectra and the relation between their integrated values, i.e. σ_ρ^2 and σ_v^2, respectively. To achieve this goal, we used a spatial fixed-scale filtering method to disentangle the laminar from the turbulent motions, producing a computative 3D distribution of turbulence. We estimated σ_ρ^2 and σ_v^2 within a spatial scale of 600 kpc, by computing the variance of the density and velocity fluctuations. A close comparison can be drawn here with Zhuravleva et al. (2014b), who studied the same relation in a sample of 6 relaxed clusters; Fig. 5.1 and 5.2 shows that these authors found a one-to-one relation between density and velocity fluctuations, across a broad range of spatial scales, asserting that the same relation might be valid in perturbed clusters as well.

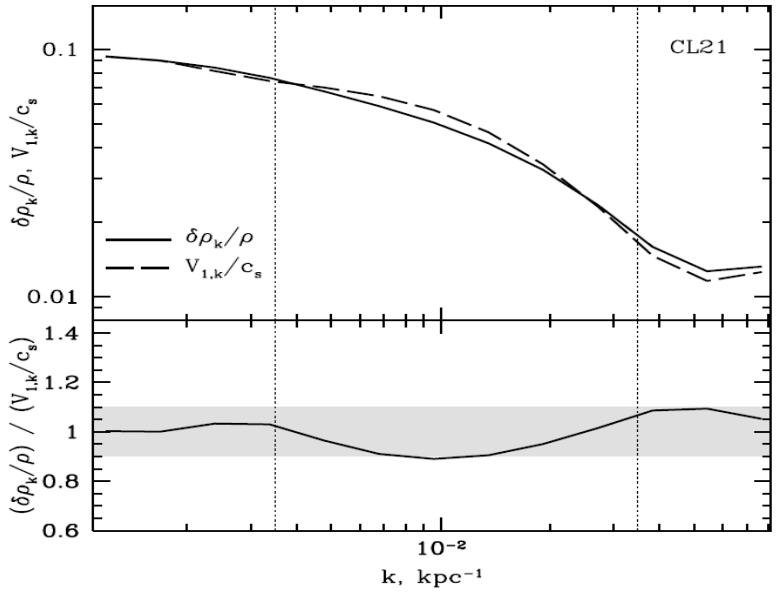

Figure 5.1: Amplitudes of density and velocity fluctuations (top panel) and their ratio (bottom panel) in a simulated cluster. Plot from Zhuravleva et al. (2014b).

The outcome of our work, compared to Zhuravleva et al. (2014b), are twofold. On one hand in our cluster sample we found that, even if the density and velocity power spectra show different slopes, the integrated power spectra result in a relation between density and velocity fluctuations. However, the spectral slopes we recover are not consistent with a one-to-one relation, and we additionally found that considering both the centroid shift and the concentration parameter, the slope depends on the dynamical state of galaxy clusters (see Table 2 and 3). However, it shall be noticed that Zhuravleva et al. (2014b) estimated the density fluctuations as the residuals of the density profile after subtracting a β - model. We also used a very similar filtering technique in which the density fluctuations was estimated after the subtraction of the density mean averaged on shells at a certain radius. In this case, we cannot define a unique fixed filtering scale, but it is reasonable to think that some filtering scales are larger than 300 kpc and some smaller. Fig. 5.2 shows that for small k values, which means large spatial scales, the one-to-one relation is still not valid, with density fluctuations being typically larger than velocity fluctuations. We obtained similar results when we estimated the density fluctuation evaluating the density mean from the 3D density radial profile (see Fig. 4.14). It is also interesting to notice that the ratio between velocity

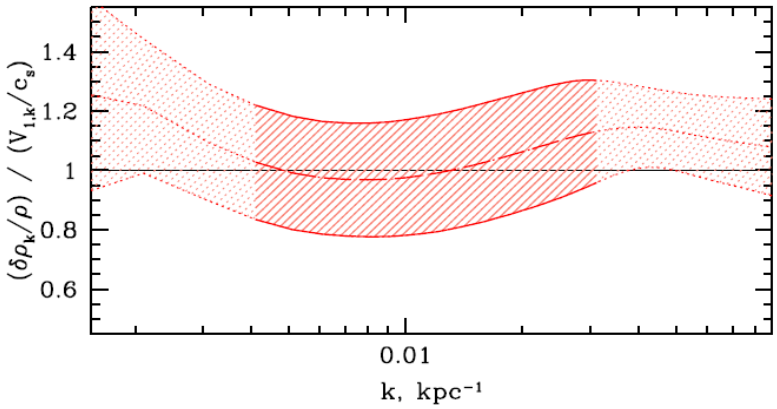

Figure 5.2: Ratio of the amplitudes of density and velocity fluctuations averaged on the cluster sample. Plot from Zhuravleva et al. (2014b).

and density fluctuations depends on the distance from the center of the cluster, as Fig 5.3 shows. In this plot, R_{vir} is the virial radius and the black points are related to relaxed clusters, while the values of the perturbed ones are shown in blue. Regardless of the dynamical state of the cluster, the ratio seems to rise as we move to larger radii. The classification is based on the centroid shift parameter.

Moreover, we investigated the role of stratification in the production of density fluctuations. To explore the balance between buoyancy and turbulence we used the Richardson number R_i, which is an estimate of the dominance of turbulence compared to gravity. We sought for a relation between the logarithmic density fluctuations and the Richardson number, following the recent work by Mohapatra et al. (2020). Figures 4.18 and 4.21 show that there is not a correlation between the two variables in our cluster sample. However, the values of the logarithmic density fluctuations we found are larger than the ones that Mohapatra et al. obtained. This big difference might be caused by the different nature of the simulation, since their setup is much more idealised, both concerning the forcing of turbulence and the absence of self-gravitating gas substructures and bulk motions. Another element of difference might be the estimation of the logarithmic density fluctuation: while the distribution function reported by Mohapatra et al. was consistent with a log-normal distribution, our distribution turned out to be different, with tails both at smallest (probably created by supersonic turbulent motions) and largest density fluctuation values (see Fig. 4.17). In this sense, the variance might not represent the best estimation of the density fluctuations.

In conclusion, the main findings of this thesis are:

- Even though Zhuravleva et al. (2014b) found a one to one relation between density and velocity turbulent fluctuations, we obtained that the mean ratio in the sample is $\left(\sigma_v^2/\sigma_\rho^2\right)^{1/2} = 0.59 \pm 016$ in the perturbed clusters (classification according to the centroid shift parameter), 0.68 ± 0.23 in the relaxed ones and that the $\delta\rho/\rho - \delta v/cs$ correlation might depend on the dynamical state of the galaxy cluster. Fig. 5.3 shows the radial dependence of the ratio. Future works may better explored the multi-parameter dependence of the underlying correlation, in clusters with a different dynamical state.

- The turbulent velocity fluctuations rather well follow the Kolmogorov theory, with a power spectrum slope consistent with -11/3, which is the Kolmogorov slope for a 3D spectrum, considering the spatial scale range 70 kpc $\lesssim$ L $\lesssim$ 350 kpc. On the other hand, gas density fluctuations present some variations in their spectral slope as we consider regions of the cluster at different radii.

- Despite the results of previous works (Federrath et al. 2008, Zhuravleva et al. 2013), the distribution function of logarithmic density fluctuations in our simulated ICM is not log-normal. This is likely be due to the presence of local supersonic turbulent motions which increase the width of the distribution, and promote the formation of higher left tail.

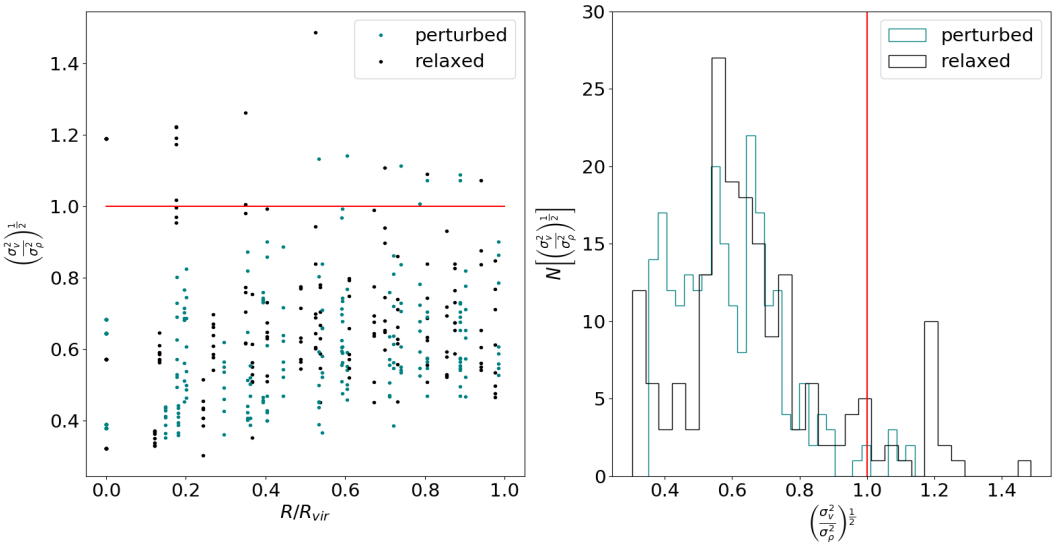

Figure 5.3: Ratio of the amplitudes of density and velocity fluctuations as function of the distance from the cluster center. The black point correspond to relaxed clusters and blue points to the perturbed ones. The classification is based on the centroid shift parameter.

- Although Mohapatra et al. (2020) found a tight relation between the logarithmic density turbulent fluctuations and the Richardson number, which takes into account the strength of the buoyancy force compared to the turbulent forcing, we could not replicate their results. The time-dependent plasma environment we analysed is more complex and no simple relation between the two variables emerged from our analysis. As Fig. 4.20 shows, we do not have a unique Mach number and some local supersonic turbulent motions might affect the result as well. This, with the likely presence of accreted clumps and filaments from the outer regions, makes the evaluation of the density fluctuations less straightforward and further refinements must be taken into account in the future works.

In summary, since a frequently used method to approach turbulence in the ICM in observations is the analysis of surface brightness fluctuations, this thesis (and other future works) provides a fundamental tool for high-resolution data analysis coming from existing (XMM-Newton, Chandra, eROSITA) and future (Athena) X-ray telescopes.

Finally, the are some further analysis we will perform in future works. First of all, we will investigate the $\sigma_\rho^2 - \sigma_v^2$ relation considering the whole volume of the galaxy clusters and a multi-parameter regression between these two variable, in order to get a full picture on this topic. Moreover, we will extend the analysis of the radial profile of the Richardson number to the entire cluster sample, in order to investigate if the Richardson number might affect the density spectra slope too. In fact, the density slope presents variations at radii larger than the virial radius, where turbulence seems to be the dominant process for gas dynamics. Another aspect that will be worth investigating in the near future is the estimation of the density fluctuations: trying to find a statistic which can be robust both in the subsonic and supersonic regime will allow us to link turbulence and density with smaller statistical uncertainties. Finally, we will produce X-ray surface brightness fluctuations maps to compare our results with present and future X-ray observational data.

List of Figures

List of Tables

References

Angelinelli M., Vazza F., Giocoli C., Ettori S., Jones T. W., Brunetti G., Brüggen M., Eckert D., 2020, MNRAS, 495, 864

Beresnyak A., Miniati F., 2016, ApJ, 817, 127

Brighenti F., Mathews W. G., 2002, ApJ, 573, 542

Brunetti G. et al., 2008, Nature, 455, 944

Brunetti G., Jones T. W., 2014, International Journal of Modern Physics D, 23, 1430007

Bryan G. L. et al., 2014, ApJS, 211, 19

Cassano R., 2010, A&A, 517, A10

Cavaliere A., Fusco-Femiano R., 1976, A&A, 500, 95

Colella P., Woodward P. R., 1984, Journal of Computational Physics, 54, 174

De Grandi S., Molendi S., 2002, ApJ, 567, 163

Dolag K., Vazza F., Brunetti G., Tormen G., 2005, MNRAS, 364, 753

Eckert D., Gaspari M., Vazza F., Gastaldello F., Tramacere A., Zimmer S., Ettori S., Paltani S., 2017, ApJ Letters, 843, L29

Eckert D. et al., 2019, A&A, 621, A40

Ettori S. et al., 2019, A&A, 621, A39

Evrard A. E., 1990, ApJ, 363, 349

Federrath C., Klessen R. S., Schmidt W., 2008, ApJ Letters, 688, L79

Feretti L., Giovannini G., Govoni F., Murgia M., 2012, The Astronomy and Astrophysics Review, 20, 54

Gaspari M., Brighenti F., D'Ercole A., Melioli C., 2011a, MNRAS, 415, 1549

Gaspari M., Churazov E., Nagai D., Lau E. T., Zhuravleva I., 2014, A&A, 569, A67

Gaspari M., Melioli C., Brighenti F., D'Ercole A., 2011b, MNRAS, 411, 349

Genel S., Bouché N., Naab T., Sternberg A., Genzel R., 2010, ApJ, 719, 229

Giodini S., Lovisari L., Pointecouteau E., Ettori S., Reiprich T. H., Hoekstra H., 2013, Science & Space Review, 177, 247

Hitomi Collaboration et al., 2016, Nature, 535, 117

Hockney R. W., Eastwood J. W., 1988, Computer simulation using particles

Kaiser N., 1986, MNRAS, 222, 323

Kim J., Ryu D., 2005, ApJ Letters, 630, L45

Kolmogorov A., 1941, Akademiia Nauk SSSR Doklady, 30, 301

Komatsu E. et al., 2011, ApJS, 192, 18

Kravtsov A. V., Vikhlinin A., Nagai D., 2006, ApJ, 650, 128

Lau E. T., Kravtsov A. V., Nagai D., 2009, ApJ, 705, 1129

Li Y. et al., 2020, ApJ Letters, 889, L1

Markevitch M., Forman W. R., Sarazin C. L., Vikhlinin A., 1998, ApJ, 503, 77

Miniati F., 2015, ApJ, 800, 60

Mohapatra R., Federrath C., Sharma P., 2020, MNRAS, 493, 5838

Norman M. L., Bryan G. L., 1999, Cluster Turbulence, Röser H.-J., Meisenheimer K., eds., Vol. 530, p. 106

Planck Collaboration et al., 2014, A&A, 571, A24

Planelles S., Schleicher D. R. G., Bykov A. M., 2016, Large-Scale Structure Formation: From the First Non-linear Objects to Massive Galaxy Clusters, Balogh A., Bykov A., Eastwood J., Kaastra J., eds., pp. 93–139

Pope S. B., 2000, Turbulent Flows. Cambridge University Press

Pratt G. W., Böhringer H., Croston J. H., Arnaud M., Borgani S., Finoguenov A., Temple R. F., 2007, A&A, 461, 71

Press W. H., Schechter P., 1974, ApJ, 187, 425

Rebusco P., Churazov E., Böhringer H., Forman W., 2006, MNRAS, 372, 1840

Reynolds C. S., Balbus S. A., Schekochihin A. A., 2015, ApJ, 815, 41

Richardson L. F., 1922, Weather prediction by numerical process. Cambridge University Press

Roediger E., Kraft R. P., Nulsen P., Churazov E., Forman W., Brüggen M., Kokotanekova R., 2013, MNRAS, 436, 1721

Ryu D., Kang H., 2003, Journal of Korean Astronomical Society, 36, 105

Sanders J. S., Fabian A. C., 2012, MNRAS, 421, 726

Sanders J. S., Fabian A. C., Smith R. K., Peterson J. R., 2010, MNRAS, 402, L11

Schindler S., Muller E., 1993, A&A, 272, 137

Schuecker P., Finoguenov A., Miniati F., Böhringer H., Briel U. G., 2004, A&A, 426, 387

Shi X., Zhang C., 2019, MNRAS, 487, 1072

Sinha N., 2013, PhD thesis

Spitzer L., 1962, Physics of Fully Ionized Gases

Sunyaev R. A., Zeldovich Y. B., 1970, APSS, 7, 3

Thomas P. A., Couchman H. M. P., 1992, MNRAS, 257, 11

Valdarnini R., 2019, ApJ, 874, 42

van Weeren R. J., de Gasperin F., Akamatsu H., Brüggen M., Feretti L., Kang H., Stroe A., Zandanel F., 2019, Science & Space Review, 215, 16

Vazza F., Brunetti G., Gheller C., 2009a, MNRAS, 395, 1333

Vazza F., Brunetti G., Gheller C., Brunino R., Brüggen M., 2011, A&A, 529, A17

Vazza F., Brunetti G., Kritsuk A., Wagner R., Gheller C., Norman M., 2009b, A&A, 504, 33

Vazza F., Jones T. W., Brüggen M., Brunetti G., Gheller C., Porter D., Ryu D., 2017, MNRAS, 464, 210

Vazza F., Roediger E., Brüggen M., 2012, A&A, 544, A103

Vikhlinin A. et al., 2009, ApJ, 692, 1033

Vikhlinin A., Markevitch M., Murray S. S., Jones C., Forman W., Van Speybroeck L., 2005, ApJ, 628, 655

Wang Q. H. S., Markevitch M., 2018, ApJ, 868, 45

Wittor D., Jones T., Vazza F., Brüggen M., 2017, MNRAS, 471, 3212

Zhuravleva I., Churazov E., Kravtsov A., Lau E. T., Nagai D., Sunyaev R., 2013, MNRAS, 428, 3274

Zhuravleva I. et al., 2014a, Nature, 515, 85

Zhuravleva I. et al., 2014b, ApJ Letters, 788, L13

ZuHone J. A., Markevitch M., Brunetti G., 2011, in American Astronomical Society Meeting Abstracts, Vol. 218, American Astronomical Society Meeting Abstracts #218, p. 408.25